

Diversity in hydrogen-rich envelope mass of type II supernovae (I): V-band light curve modeling

Qiliang Fang (方其亮),^{1,2} Keiichi Maeda,² Haonan Ye (叶浩楠),² Takashi J. Moriya,^{1,3,4} and Tatsuya Matsumoto^{2,5}

¹National Astronomical Observatory of Japan, National Institutes of Natural Sciences, 2-21-1 Osawa, Mitaka, Tokyo 181-8588, Japan

²Department of Astronomy, Kyoto University, Kitashirakawa-Oiwake-cho, Sakyo-ku, Kyoto 606-8502, Japan

³Graduate Institute for Advanced Studies, SOKENDAI, 2-21-1 Osawa, Mitaka, Tokyo 181-8588, Japan

⁴School of Physics and Astronomy, Monash University, Clayton, Victoria 3800, Australia

⁵Hakubi Center, Kyoto University, Yoshida-honmachi, Sakyo-ku, Kyoto 606-8501 Japan

ABSTRACT

We conduct a systematic study on the light curves of type II supernovae (SNe II) to investigate how they are affected by the physical properties of the progenitor and the nature of the explosion. The calculations of pre-supernova evolution, the launch of the explosion, and the light curve are carried out by MESA and STELLA. Our study encompasses a wide range of zero-age-main-sequence (ZAMS) masses ($10-20 M_{\odot}$), wind mass-loss rates (which control the range of hydrogen-rich envelope mass to be $3-12 M_{\odot}$), explosion energies ($0.1-2.5 \times 10^{51}$ erg), and ^{56}Ni masses ($0-0.15 M_{\odot}$). Our analyses reveal that when the explosion energy is fixed, the light curve is primarily determined by the properties of the hydrogen-rich envelope, despite the large variation in the ZAMS masses. The dependencies of the light-curve characteristics on the envelope mass, radius, and explosion energy are investigated, and we establish the scaling relations connecting these quantities. We further derive a formula that corrects for effects of the ^{56}Ni heating based on observables. Using the derived equations, we develop a method that can constrain the envelope mass with uncertainty within $1 M_{\odot}$ based on photometry. This method is applied to a large sample of ~ 100 SNe II, which reveals a considerably broader range of the envelope masses estimated from observables as compared to those predicted by single star models evolving with standard stellar wind; this finding indicates that a large fraction of SNe II experience substantial mass-loss beyond the standard mass-loss prescription prior to their explosions, highlighting the uncertainties involved in the massive star evolution and pre-SN mass-loss mechanism.

1. INTRODUCTION

Core-collapse supernovae (CCSNe) are catastrophic explosions that are believed to occur in massive stars (typically with ZAMS mass $M_{\text{ZAMS}} \gtrsim 8 M_{\odot}$) once the fuel in their cores is exhausted. CCSNe exhibit a wide range of observable characteristics, and a primary goal of modern stellar physics is to establish a connection between this diversity and the massive progenitor stars that give rise to them.

Type II supernovae (SNe II), which are the most commonly observed CCSNe, show hydrogen features in their spectra, indicating the presence of a massive hydrogen-rich envelope in their progenitors (Filippenko 1997; Gal-Yam 2017; Modjaz et al. 2019). SNe II are characterized by the plateau phase in their light curves. During this phase, the brightness remains almost constant for approximately 50 to 100 days due to the recombination of the hydrogen in the envelope. Following the expansion of the ejecta, the photosphere gradually descends inward and finally reaches to the bottom of the hydrogen-rich

envelope, resulting in the sudden drop of the light curve brightness. The ejecta then enters so called the nebular phase. Pre-explosion photometry confirms the red supergiants (RSGs) as progenitors for a limited number of SNe II, where the ZAMS masses of these progenitors are suggested to be $\lesssim 17 M_{\odot}$ (Van Dyk et al. 2003, 2012a,b, 2019, 2023a,b; Smartt et al. 2004; Maund & Smartt 2005a; Maund et al. 2005b, 2013, 2014a,b; Li et al. 2006; Fraser et al. 2010, 2011, 2012, 2014; Crockett et al. 2011; Elias-Rosa et al. 2011; Kochanek et al. 2012, 2017; Tomasella et al. 2013; O’Neill et al. 2019; Rui et al. 2019; Sollerman et al. 2021; Jencson et al. 2023; Kilpatrick et al. 2023a). The lack of progenitors with $M_{\text{ZAMS}} > 17 M_{\odot}$, known as the RSG problem, presents a challenge (Smartt 2009, 2015; Walmswell & Eldridge 2012; Eldridge et al. 2013; Meynet et al. 2015; Davies & Beasor 2018; Hiramatsu et al. 2021a; Strotjohann et al. 2023). However, determining M_{ZAMS} based on pre-explosion photometry is often uncertain due to various factors such as the lack of multi-band photometry, the uncertainties in reddening estimates, and the limitations

of stellar evolution models. Further, the progenitor before the explosion is usually too dim for deep imaging, making pre-SN photometry only feasible for a limited number of SNe II (Smartt 2009).

Radiation hydrodynamics and radiative transfer calculations are frequently utilized to constrain the nature of SNe II in the literature (See for example Morozova et al. 2015; Martinez et al. 2020). This approach involves the evolution of the progenitor models with varying M_{ZAMS} up to the onset of core-collapse, followed by the deposition of energies into their cores to trigger the explosions. Sometimes non-evolutionary progenitor models are employed. The initial density and chemical composition distributions, along with their masses and radii, of these models are set as free parameters (Bersten et al. 2011; Martinez & Bersten 2019). Following the construction of the progenitor models, radioactive ^{56}Ni is manually introduced into the ejecta, with variations in their amounts and distributions. The light curves of these models are then calculated and compared with those from observation, which allows us to extract the properties of the progenitor and the nature of the explosion (Morozova et al. 2016, 2017, 2018; Martinez et al. 2022a,b,c; Subrayan et al. 2023; Zha et al. 2023).

While this approach is frequently applied, it has several limitations. The plateau phase of the light curve is driven by the recombination of hydrogen in the envelope, making its characteristics primarily determined by the properties of the hydrogen-rich region (Popov 1993; Kasen & Woosley 2009; Dessart & Hillier 2019). Inferring M_{ZAMS} from light curve modeling relies on the underlying assumption of the unique relation between the properties of the envelope and M_{ZAMS} . However, there are several uncertainties involved in establishing this relation: (1) The formula that describes the RSG mass-loss rate, which is a function of the star’s properties (e.g., mass, radius, luminosity, metallicity), is empirically derived from observation and involves many uncertainties in both observation and theory (Reimers 1975; Lamers 1981; de Jager et al. 1988; Nieuwenhuijzen & de Jager 1990; Kudritzki & Puls 2000; Nugis & Lamers 2000, 2002; Willson 2000; Vink et al. 2001; Maeder & Meynet 2001; Schröder & Cuntz 2005; van Loon et al. 2005; Eldridge & Vink 2006; Beasor et al. 2020; Vink & Sabhahit 2023). The accuracy of the RSG mass-loss rate when applied to the progenitors of SNe II therefore remains uncertain; (2) massive stars can be born in binary systems, where the amount of envelope stripping is primarily determined by the orbital parameters such as the mass ratio or the separation between the primary and secondary stars. In this case, the dependence of envelope mass on M_{ZAMS} becomes invisible (Heger et al.

2003; Eldridge et al. 2008; Yoon et al. 2010; Smith et al. 2011; Sana et al. 2012; Groh et al. 2013; Smith 2014; Yoon 2015; Yoon et al. 2017; Ouchi & Maeda 2017; Eldridge et al. 2018; Fang et al. 2019; Gilkis & Arcavi 2022; Chen et al. 2023; Drout et al. 2023; Ercolino et al. 2023; Fragos et al. 2023; Hirai 2023; Matsuoka & Sawada 2023; Sun et al. 2023; Dessart et al. 2024, among many others).

To illustrate the uncertainties discussed above, Dessart & Hillier (2019) calculated the light curves of a grid of progenitor models with the same envelope mass ($M_{\text{Henv}} \sim 8 M_{\odot}$) and explosion energy (1.25×10^{51} erg) but different M_{ZAMS} (12 to $25 M_{\odot}$), and the light curves at the plateau phase were found to be similar for all models. Goldberg et al. (2019) also revealed that models with varying ejecta masses M_{eje} can produce similar light curves (M_{eje} includes the masses of the material below the hydrogen-rich envelope, which can be comparable to M_{Henv} if M_{ZAMS} is large). These works highlight the non-uniqueness of progenitor properties inferred from light-curve modeling.

In this work, we extend the analysis outlined in Dessart & Hillier (2019). We evolve progenitor models with M_{ZAMS} ranging from 10 to $20 M_{\odot}$, resulting in the envelope mass ranging from 3 to $14 M_{\odot}$ through manually enhance or depress the normal (standard) mass-loss rates. These progenitors are exploded by manually injecting varied amounts of energies, and the corresponding light curves are calculated. Based on the survey of this light curve model grid, we conclude that, light curve modeling, in the absence of prior knowledge regarding the mass-loss history, does not provide informative constraints on the ejecta mass or M_{ZAMS} . However, it does allow a precise estimation of the envelope mass within an uncertainty of $1 M_{\odot}$. The inferred distribution of the envelope masses for a sample of SNe II reveals a considerably broader range compared to the predictions of single star models evolving with the standard stellar-wind prescription. This inconsistency highlights the uncertainty involved in the mass-loss history before the explosion.

This paper is organized as follow. In §2, we introduce the numerical approach, including the evolution of a grid of progenitors and their light curves. In §3, we present the sample survey for the obtained light curves, and establish the scaling relations between the characteristics of the light curves (plateau duration and magnitude) and the hydrogen-rich envelope mass, the radius and explosion energy for models without ^{56}Ni . Based on these relations, we establish a method to constrain the envelope mass within uncertainty of $1 M_{\odot}$. The effects of the ^{56}Ni heating are also discussed. In §4, the results from §3 are applied to observational data. We derive

the distribution of hydrogen-rich envelope masses for a large sample of SNe II ($N \sim 100$), and discuss its implications for massive star evolution and pre-SN mass-loss mechanism(s). §5 discusses the factors that may affect the results in §3. The conclusions are presented in §6.

2. NUMERICAL SETUP

2.1. Progenitor calculation

The SN progenitor models are calculated using the one-dimensional stellar evolution code, Modules for Experiments in Stellar Astrophysics (MESA, Paxton et al. 2011, 2013, 2015, 2018, 2019). We start with MESA version r22.11.1 test suite `example_make_pre_ccsn` to create non-rotating, solar metallicity progenitor models. The ZAMS masses are selected to be 10, 12, 15, 18 and 20 M_{ZAMS} , which encompass the typical mass range for SNe II progenitors (see for example Smartt 2015; Valenti et al. 2016; Davies & Beasor 2018, 2020). For the fiducial models, we employ the same mixing scheme as Martinez et al. (2020), i.e., Ledoux criterion for convection, mixing length parameter $\alpha_{\text{MLT}} = 2.0$, exponential overshooting parameters $f_{\text{ov}} = 0.004$ and $f_{\text{ov},0} = 0.001$, semi-convection efficiency $\alpha_{\text{sc}} = 0.01$ (Farmer et al. 2016), thermohaline mixing coefficient $\alpha_{\text{th}} = 2$ (Kippenhahn et al. 1980) and Dutch wind scheme (de Jager et al. 1988; Vink et al. 2001; Glebbeek et al. 2009). However, unlike Martinez et al. (2020) where the Dutch wind efficiency η is held constant at 1.0, in this work, η is allowed to freely vary, i.e., the mass-loss rate \dot{M} is

$$\dot{M} = \eta \dot{M}_{\text{Dutch}}, \quad (1)$$

and different hydrogen-rich envelope masses M_{Henv} for each M_{ZAMS} are thus obtained, which ranges from 3 to 14 M_{\odot} . Here \dot{M}_{Dutch} is the Dutch wind mass-loss rate. We note here that, for progenitor models with $M_{\text{ZAMS}} = 10$ or 12 M_{\odot} , η would required to be as large as 6.0 to 8.0 to get small M_{Henv} at 3-4 M_{\odot} , which does not seem to be realistic. Therefore, we consider the variation in η as a phenomenological approach to remove the hydrogen-rich envelope, rather than directly connecting it with any mass-loss mechanism. Except for this slow mass-loss scheme controlled by η , we also consider the mass-loss scheme where the mass is removed instantaneously (e.g., driven by unstable binary mass-transfer or violent activity of massive stars; see, e.g., Smith 2014 for a review), aiming to investigate the effect of the mass-loss timescale. Rather than self-consistently modeling these highly uncertain mass-loss mechanisms, progenitors models are evolved to the depletion of helium in the core, with $\eta = 0.0$. Subsequently, we use the command `relax_mass_to_remove_H_env`

to remove the hydrogen-rich envelope, with maximum mass-loss rate held constant at $10^{-2} M_{\odot} \text{yr}^{-1}$ (`lg_max_abs_mdot = -2`). The stripped models are then further evolved to the depletion of carbon in the core fixing $\eta = 0.0$. Our own experiment show that ranging `lg_max_abs_mdot` from -1 to -4 will not affect the final radius. The residual M_{Henv} is controlled by the command `extra_mass_retained_by_remove_H_env` and ranges from 3 to 14 M_{\odot} in steps of 1 M_{\odot} (the upper limit of the residual envelope mass depends on M_{ZAMS}). We note here that, after the stripping procedure, the subsequent carbon burning phase will increase the helium core mass by 0.02 to 0.2 M_{\odot} , and M_{Henv} is slightly decreased according, so the final M_{Henv} is not exactly the same as `extra_mass_retained_by_remove_H_env`. However, such difference is small. The time scale for the stripping procedure is $\sim 10^4$ years, which is short compared with the time scale of the mass-loss controlled by η ($\sim 10^6$ years for $M_{\text{ZAMS}} = 15 M_{\odot}$), therefore can be considered as occurring instantaneously. Hereafter the mass-loss controlled by Dutch wind efficiency η is referred to as wind scheme, while the one controlled by `relax_mass_to_remove_H_env` is referred to as strip scheme. Specially, we refer the Dutch wind scheme with $\eta = 1.0$ as the *standard* stellar wind.

With these setups, the progenitor models are evolved from pre-main-sequence to the depletion of carbon in the core. The models are not evolved to the core collapse in this study for the reasons below: (1) For models with $M_{\text{ZAMS}} \leq 12 M_{\odot}$, the calculation of the advanced fusions becomes computationally expensive and time-consuming. Some of the models develop off-center flames, leading to convergence problem during core oxygen burning phase. In fact, the products of the advanced fusions are mostly excised when the explosions are phenomenologically triggered (§2.2) and are not relevant to this study; (2) this study focuses on the plateau phase of SNe II light curves, which is primarily determined by the explosion energy and the properties of the hydrogen-rich envelope. After the carbon depletion, the outermost envelope is detached from the subsequent core evolution. A detailed discussion on this topic is deferred to §5.2.

The progenitor properties at the point of the carbon depletion are summarized in Table 1, and are plotted in Figure 1. In general, the radii of the progenitors range from 500 to 1100 R_{\odot} , and the removal of the hydrogen-rich envelope will not significantly affect the radius once M_{ZAMS} is fixed.

2.2. Hand-off to STELLA

M_{ZAMS}	η	M_{Henv}	R	$M_{\text{He core}}$
10	0.0	7.37	511	2.62
	1.0	6.94	509	2.50
	Wind scheme	4.18-7.37	482-512	1.68-2.62
	Strip scheme	2.98-7.00	523-594	2.63-2.65
12	0.0	8.91	606	3.09
	1.0	7.97	616	3.09
	Wind scheme	3.23-8.91	606-633	2.79-3.09
	Strip scheme	2.94-7.95	619-709	3.09-3.10
15	0.0	10.66	836	4.34
	1.0	8.76	857	4.30
	Wind scheme	3.42-10.65	836-921	4.17-4.36
	Strip scheme	2.89-9.89	847-957	4.34-4.35
18	0.0	12.30	1010	5.70
	1.0	8.06	1008	5.58
	Wind scheme	4.16-12.30	947-1027	5.28-5.70
	Strip scheme	2.91-11.89	961-1029	5.68-5.69
20	0.0	13.29	1126	6.71
	1.0	7.92	1035	6.65
	Wind scheme	3.35-13.29	980-1126	6.53-6.71
	Strip scheme	2.75-12.75	934-1125	6.71-6.72

Table 1. Summary of the progenitor properties. Columns: ZAMS mass, mass loss scheme, hydrogen-rich envelope mass, stellar radius and helium core mass. The masses and radii are in solar unit.

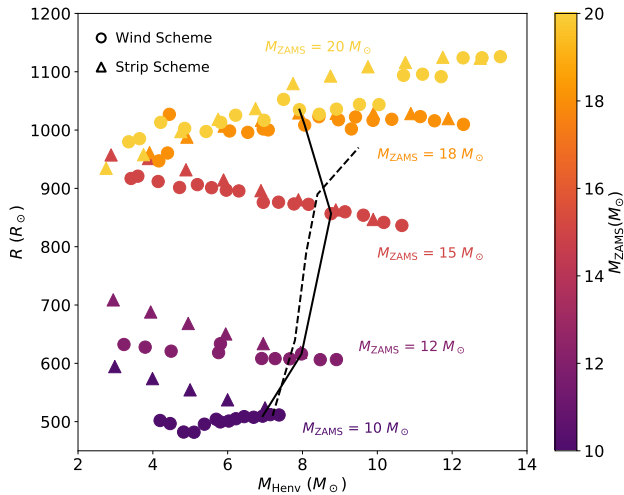


Figure 1. The hydrogen-rich envelope mass M_{Henv} and the radius R of the progenitor models in this work. Individual models are color coded by M_{ZAMS} . The solid and dashed lines represent the $M_{\text{Henv}}-R$ relation predicted by the models with $\eta = 1.0$ in this work and the *Kepler* models (Sukhbold et al. 2016, which are applied in Moriya et al. 2023) respectively.

For handing-off the hydrostatic progenitor models to *STELLA* for light curve calculations, we closely follow the test suite *ccsn_IIP* to trigger the explosions. This simulation includes two procedures; the energy injection and the shock propagation. To perform the mass-cut that mimics the compact remnant formation, we evolve the progenitor models with $M_{\text{ZAMS}} = 12, 15, 18, 20 M_{\odot}$ and $\eta = 1.0$ to the point when iron core infall speed exceeds 100 km s^{-1} , i.e., the onset of core-collapse. The inner mass coordinate where entropy/baryon $= 4 k_{\text{B}}$ are $1.4, 1.6, 1.9$ and $2.0 M_{\odot}$ respectively, which are subsequently selected as the mass-cuts for models with the same M_{ZAMS} but different M_{Henv} (Ertl et al. 2016), as the loosely-attached envelope hardly affect the evolution of the inner core. For models with $M_{\text{ZAMS}} = 10 M_{\odot}$, the mass-cut is $1.2 M_{\odot}$, aligned with the mass coordinate where entropy/baryon $= 4 k_{\text{B}}$ when the model with $M_{\text{ZAMS}} = 10 M_{\odot}$ and $\eta = 1.0$ is evolved to the core carbon depletion. As long as we are only interested in the plateau phase of the SNe II, the small variation in the mass-cut is indeed not important.

After the remnant is removed, the explosion energy is manually deposited in the inner $0.2 M_{\odot}$ to induce the strong shock and trigger the explosion. A number of explosion models are calculated for each progenitor model, with the asymptotic energy (i.e., the energy stored in the expanding ejecta) ranging from 0.5 to 2.5×10^{51} erg (in 0.5×10^{51} erg steps). Hereafter we refer to 1×10^{51} erg as 1 foe. For models with $M_{\text{ZAMS}} = 10, 12$ and $15 M_{\odot}$, we additionally calculate explosions with the asymptotic energy of 0.3 foe. For models with $M_{\text{ZAMS}} = 10$ and $12 M_{\odot}$, we further calculate low-energy events with the asymptotic energy $= 0.1$ foe. In the following text, we use the term ‘explosion energy’ to refer to the asymptotic energy for convenience.

Strong shock is generated following the launch of the explosion, which then propagates through the envelope. During the shock propagation, the infalling material is removed by turning on the command `fallback_check_total_energy`. After the shock front reaches to $0.05 M_{\odot}$ below the stellar surface, the calculation is halted. At this point, we manually excise materials with fallback velocity larger than 500 km s^{-1} and uniformly distribute radioactive ^{56}Ni below the inner boundary of the hydrogen-rich envelope. The mass of ^{56}Ni (M_{Ni}) varies from 0.00 to $0.10 M_{\odot}$ with $0.01 M_{\odot}$ increments. Additional models with $M_{\text{Ni}} = 0.001, 0.005, 0.008, 0.12$ and $0.15 M_{\odot}$ are also calculated. Both the amount and the distribution of ^{56}Ni play roles in shaping the light curve characteristics (Kasen & Woosley 2009; Bersten et al. 2011; Moriya et al. 2016). Observationally, there is evidence that a fraction of ^{56}Ni is mixed

into the hydrogen-rich envelope. It has long been realized that substantial material mixing during the explosion is required to produce the observed smooth SNe II light curves. To mimic this effect, we apply the artificial ‘boxcar’ averaging by setting the boxcar size to be 10% of the helium core mass, which then runs through the ejecta for 4 times to average the mass fractions of the different elements (Kasen & Woosley 2009; Morozova et al. 2015).

With the above setups, the models are hand-off to STELLA, an one-dimensional multi-frequency radiation hydrodynamics code (Blinnikov et al. 1998, 2000, 2006), for the calculation of the light curves. We set 800 spatial zones and 40 frequency bins. No circumstellar material (CSM) is introduced. Models that take a long time to converge are simply discarded, as we are only interested in the bulk statistics of the model grid.

3. RESULT

In this section, we start with the sample survey of models without ^{56}Ni , which serve as the reference models for the following discussions. We investigate how the basic parameters, i.e., the hydrogen-rich envelope mass M_{Henv} , radius R , and the explosion energy E , affect the light curve characteristics. Especially, we focus on the duration and the magnitude of the plateau, and derive the scaling relations connecting these observables with the physical properties of the explosion. Based on these scaling relations, we establish a method to accurately constrain M_{Henv} . The effects of the ^{56}Ni heating on the light curve characteristics are also discussed.

3.1. Sample survey

We first focus on models without ^{56}Ni . For the model grid considered in this work, the duration of the plateau ranges from 40 to 120 days, with the peak magnitudes varying from -14.5 to -18.2 mag. The light curve characteristics are primarily determined by M_{Henv} , R and E . In general, large explosion energy and small hydrogen-rich envelope mass leads to bright and short plateau. While large radius increases the plateau magnitude, the duration is hardly affected.

To be more specific, we compare the progenitor models with different M_{ZAMS} but similar M_{Henv} . Figure 2 shows the light curves of these models, all with a fixed explosion energy $E = 1$ foe. When M_{Henv} is fixed, the duration of the plateau is quite similar, while models with larger surface radii tend to exhibit brighter plateaus as expected (Popov 1993; Kasen & Woosley 2009; Dessart et al. 2013; Dessart & Hillier 2019). The result in this work expands the scope of what was discussed in Dessart & Hillier (2019), where the light curves of models with

$M_{\text{ZAMS}} = 12$ to $25 M_{\odot}$ and $M_{\text{Henv}} \sim 8.0 M_{\odot}$ were discussed. They concluded that, with fixed M_{Henv} and E , the resulting light curves are very similar despite the wide range of M_{ZAMS} of the progenitors. They also found that the variety in the radius contribute to the bolometric luminosity of the plateau, but such difference is too small to allow for unambiguous inference on the M_{ZAMS} of the progenitors, considering the uncertainties of distances and extinctions.

Furthermore, models with their hydrogen-rich envelope stripped by different mass-loss schemes are compared in Figure 2. Although the timescale for mass-loss differs, when M_{Henv} and E are the same, the light curves appear similar, losing memory of the exact mass-loss history. Therefore, in the following text, we do not attempt to distinguish the models of wind scheme and strip scheme.

The above discussion implies the light curves of SNe II at plateau phase provide limited information regarding M_{ZAMS} of their progenitors and the mass-loss mechanism. We demonstrate that such degeneracy is valid for the typical range of M_{Henv} of SNe II (3 to $14 M_{\odot}$; see for example Hiramatsu et al. 2021a).

In the literature, M_{ZAMS} of SNe II progenitors are usually determined by fitting the observed light curve to a large grid of model light curves generated from progenitors exploded by a wide range of explosion energies (see for example Morozova et al. 2018; Martinez et al. 2020). However, as discussed above (also Dessart & Hillier 2019), the SNe II light-curve characteristics, i.e., the duration and the magnitude of the plateau, are primarily determined by the properties of the hydrogen-rich envelope, rather than directly associated with the inner helium-core. Measuring M_{ZAMS} of the progenitor by light curve modeling relies heavily on the correlation between M_{Henv} and M_{ZAMS} predicted by the *standard* wind mass-loss. However, the RSG mass-loss rates are not well constrained and the mass-loss mechanism (single star versus binary evolution) is not clear. There is no unique association between M_{Henv} and M_{ZAMS} . A detailed discussion on this topic is deferred to §4.

3.2. Scaling relations

The scaling relations between the light-curve characteristics and the properties of the progenitor are useful to constrain the nature of SNe II. In the literature, ejecta mass (M_{eje}), progenitor radius (R) and the explosion energy (E) are frequently employed as independent variables. Although other quantities, for example, opacity of the envelope (κ), ionization temperature of hydrogen (T_1) or the helium fraction in the envelope (X_{He}) are sometimes involved in deriving the scaling relations

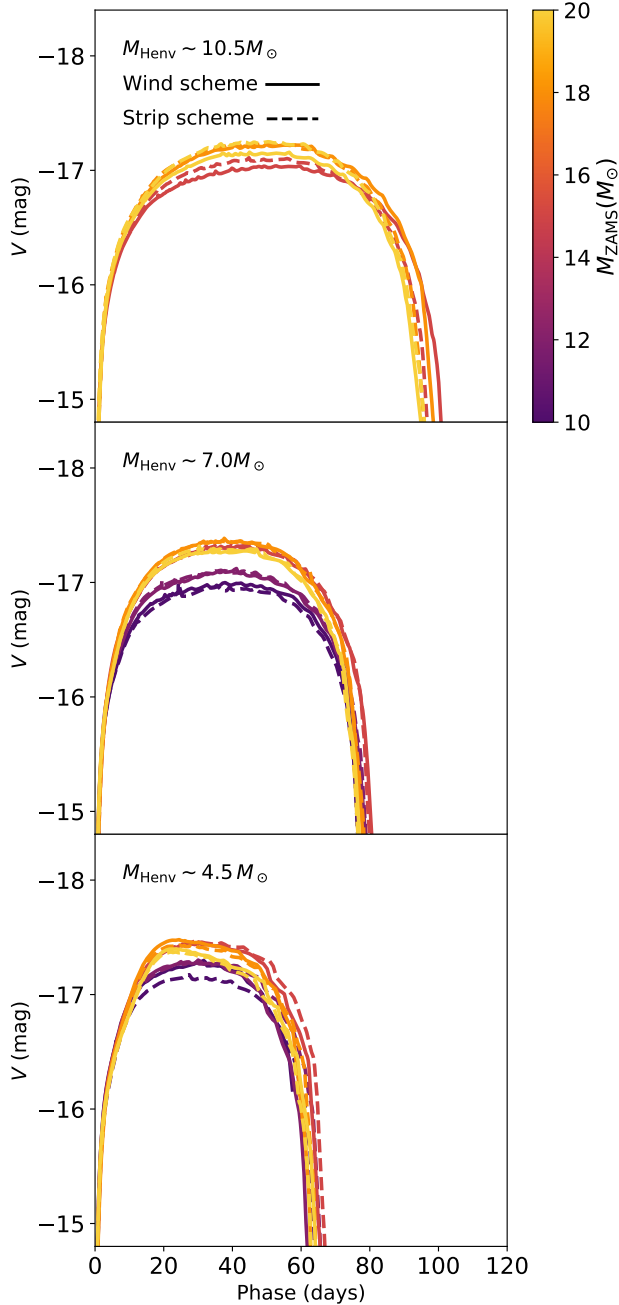


Figure 2. The comparison between the V -band light curves of progenitors with different M_{ZAMS} but the similar M_{Henv} and the same E (1 foe). From top to bottom panel: $M_{\text{Henv}} = 10.5, 7.0, 4.5 M_{\odot}$. The light curves of the models evolved with wind scheme and strip scheme are labeled by solid and dashed lines respectively.

(Popov 1993; Kasen & Woosley 2009), they are of secondary importance, and most of the analysis focus on M_{eje} , R and E (Sukhbold et al. 2016; Goldberg et al. 2019).

Based on the analytical model where the effects of radiative diffusion and hydrogen recombination are included, Popov (1993) derived the scaling relations for the nickel-free models;

$$\begin{aligned} V_{\text{p},0} &\sim -1.67 \log R + 1.25 \log M_{\text{eje}} - 2.08 \log E \\ \log t_{\text{p},0} &\sim 0.17 \log R + 0.57 \log M_{\text{eje}} - 0.17 \log E. \end{aligned} \quad (2)$$

Here, $V_{\text{p},0}$ and $t_{\text{p},0}$ are the magnitude and duration of the plateau in V -band without radioactive heating. Kasen & Woosley (2009) also reached to the similar results.

It is controversial as to which of the ejecta mass or the hydrogen-rich envelope mass should be used as an independent variable when applying the scaling relations of Popov (1993). For example, Sukhbold et al. (2016) employed M_{Henv} , while Goldberg et al. (2019) suggested to use M_{eje} after finding some hydrogen elements are mixed deeply into the interior of the star due to Rayleigh Taylor instability (RTI). In this work, we employ the artificial ‘boxcar’ average to mimic large scale mixing, which is frequently adopted in SN II light curve modeling (Kasen & Woosley 2009; Morozova et al. 2015). Based on this scheme, the hydrogen-rich envelope is only weakly mixed into the inner region and models with the same M_{Henv} have very similar light curves despite their large difference in M_{eje} , as demonstrated in §3.1. We therefore adopt M_{Henv} rather than M_{eje} as the independent variable throughout this work.

We start with measuring the plateau magnitudes and duration of the V -band light curves in our model grid. There are several methods available to define the plateau duration, based on either theoretical models or observables. For example, Goldberg et al. (2019) defined t_{p} as the phase when the opacity of the inner boundary of the ejecta drops to $\tau=10$ ($t_{\tau=10}$). Motivated by observation, Valenti et al. (2016) proposed to fit the light curves by the function

$$V(t) = \frac{A_0}{1 + e^{(t-t_{\text{p}})/W_0}} + P_0 \times t + M_0. \quad (3)$$

Here t_{p} defines the plateau duration, and other parameters together control the light-curve shape. The readers may refer to Valenti et al. (2016) for more details. However, this function requires the presence of a radioactive tail, and cannot produce reasonable fit to our reference models without ^{56}Ni . We therefore employ a simple method to measure t_{p} , which is determined by the phase when the V -band magnitude drops by 1 mag from the peak. We compare t_{p} measured in this way with $t_{\tau=10}$, and find good agreement. In the following, the plateau duration t_{p} is defined in this way, and $t_{\text{p},0}$ represents the measurements for the ^{56}Ni -free models.

In the literature, the magnitude (or luminosity) at 50 days after the shock breakout (SBO), V_{50} , is used to represent the plateau magnitude. However, for events with a very short plateau, V_{50} is not well defined. In some extreme cases, the duration of the plateau is even shorter than 50 days. In this work, we measure the plateau magnitude V_p at $t = 0.5 \times t_p$, i.e., the midpoint of the plateau. At this point, the magnitude is hardly affected by the presence of the circumstellar material (CSM) around the progenitor (Morozova et al. 2017; except for the case when the CSM is massive and extended) or by the ^{56}Ni heating. Similarly, $V_{p,0}$ represents the measurements for the ^{56}Ni -free models.

By fitting $V_{p,0}$ and $t_{p,0}$ with M_{Henv} , R and E being independent variables, we establish the scaling relations for the models in this work as follows;

$$\begin{aligned} V_{p,0} &\sim -1.07 \log R + 0.78 \log M_{\text{Henv}} - 1.98 \log E \\ \log t_{p,0} &\sim 0.02 \log R + 0.55 \log M_{\text{Henv}} - 0.17 \log E. \end{aligned} \quad (4)$$

Figure 3 illustrates the accuracy of Equation 4. Notably, the dependence of $t_{p,0}$ on R , as determined in this work (see also Lisakov et al. 2017 based on CMFGEN modeling), is much weaker than that predicted by Popov (1993) and Kasen & Woosley (2009).

As emphasized by Kasen & Woosley (2009), the relation between the radius R and the ejecta mass M_{eje} (or the hydrogen-rich envelope mass M_{Henv}) predicted by the stellar evolution model naturally contributes to Equation 4. However, by adjusting the wind efficiency η , we derive a grid of models with comparable R but different M_{Henv} (Table 1 and Figure 1). The relation between R and M_{Henv} is eliminated, and the effects of these two quantities on the light curve characteristics are therefore constrained independently.

3.3. Indicator of hydrogen-rich envelope mass

From the previous sections, we show that the properties of SNe II light curves are primarily determined by the hydrogen-rich envelope and the explosion energy. Little information on the progenitor M_{ZAMS} can be extracted without a well-constrained mass-loss scheme. However, M_{Henv} itself is an important quantity that can be used to test the mass-loss scheme in massive star evolution (§4). In this section, our aim is to establish a measurement of M_{Henv} that can be applied to observation.

We start with the investigation on how the light curve characteristics, $V_{p,0}$ and $t_{p,0}$ defined above, are affected by M_{Henv} . We note from §3.2 that an increase in the explosion energy E leads to a decrease in $t_{p,0}$ (longer duration) and an increase of $V_{p,0}$ (brighter plateau).

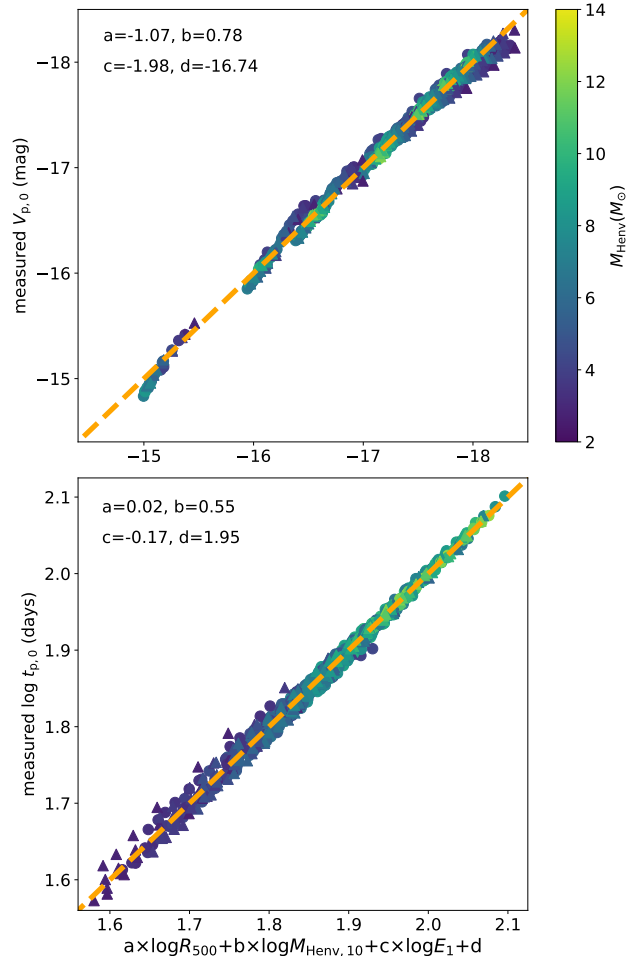


Figure 3. The accuracy of Equation 4 for plateau magnitude ($V_{p,0}$, upper panel) and duration ($t_{p,0}$, lower panel). Here, R_{500} , $M_{\text{Henv},10}$ and E_1 are R , M_{Henv} and E in the units of $500 R_{\odot}$, $10 M_{\odot}$ and 1 foe . The dashed line is one-to-one correspondence. The models are color coded by their M_{Henv} , with gradual increase of M_{Henv} from the blue end to the green end.

Therefore inferring M_{Henv} solely from $V_{p,0}$ (see for example Barker et al. 2022, 2023) or $t_{p,0}$ (see for example Gutiérrez et al. 2017a,b) is not feasible without assuming a relation between explosion energy E and the properties of the hydrogen-rich envelope. This assumption, however is not necessarily justified, as the explosion mechanism is closely related to the properties of the innermost core (Ertl et al. 2016; Burrows & Vartanyan 2021), but has little to do with the outermost envelope that is decoupled from the rapid core evolution in the final years of the massive star. As shown in the upper panel of Figure 4, if E is adjusted to produce the light curves with the same plateau duration $t_{p,0}$, the model with larger M_{Henv} is brighter. Similarly, the model with larger M_{Henv} will have longer plateau duration if E is

modified such that the light curves have the same magnitude $V_{p,0}$. This behavior suggests that, by carefully adjusting E to normalize the sample of SNe II light curves to have the same $t_{p,0}$, their plateau magnitudes $V_{p,0}$ can serve as the measurements of the M_{Henv} .

Motivated by the above discussion, we investigate the relation between $V_{p,0}$ and $t_{p,0}$, a method frequently employed to constrain the nature of transients (Kasen & Woosley 2009; Villar et al. 2017; Khatami & Kasen 2023). The result is shown in Figure 4, which reveals several distinct features: (1) models with lower M_{Henv} occupy the region of smaller $t_{p,0}$, irrespective of the variation in M_{ZAMS} ; (2) for all the progenitor models, they follow almost the same $V_{p,0}$ - $t_{p,0}$ scaling relation when E varies, i.e., $V_{p,0} \propto 11.65 \times \log t_{p,0}$ (The dotted lines).

Scaling analysis readily explains the two features: (1) From Equation 4, for a progenitor with given envelope properties (i.e., given M_{Henv} and R), the range of E , i.e., 0.1 - 2.5 foe, will create 0.24 dex difference in $t_{p,0}$, smaller than the 0.40 dex difference created by the variation in M_{Henv} , which ranges from ~ 3 to $14 M_{\odot}$. To have the same $t_{p,0}$, the model with the lowest M_{Henv} is required to explode with E lower by 2.4 dex than that of the model with the largest M_{Henv} , a difference much larger than the range of E considered in this work (~ 1.4 dex). Hence, models with small M_{Henv} occupy the region of small $t_{p,0}$; (2) By eliminating E in Equation 4, we derive

$$V_{p,0} - 11.65 \log t_{p,0} \sim -1.30 \log R - 7.19 \log M_{\text{Henv}}, \quad (5)$$

which explains the $V_{p,0}$ - $t_{p,0}$ scaling relation.

Kasen & Woosley (2009) investigated the $t_{p,0}$ - $V_{p,0}$ relation, where a tight correlation with 0.4 mag scatter is discerned (see also Sukhbold et al. 2016; Zha et al. 2023 for more recent studies). In this work, we find that the scatter level of this relation strongly depends on the assumed mass-loss prescription. For models with $\eta = 1.0$ (standard wind), we find a similar $t_{p,0}$ - $V_{p,0}$ relation with Kasen & Woosley (2009):

$$V_{p,0} = -15.94 + 0.06 \times (t_{p,0} - 100), \quad (6)$$

as specially labeled the pink stars in Figure 4. The scatter, which is 0.3 mag, is small because the range of M_{Henv} predicted by standard wind is narrow (Table 1). If all the models in the grid are brought into analysis, the $V_{p,0}$ - $t_{p,0}$ relation no longer exists due to the large scatter created by the wide range of M_{Henv} .

Motivated by Equation 5, we introduce a new quantity V_{100} , i.e., $V_{p,0}$ when the plateau duration is 'stretched' to be 100 days by adjusting the explosion energy E , as

$$V_{100} = V_{p,0} - 11.65 \times \log \frac{t_{p,0}}{100 \text{ days}}. \quad (7)$$

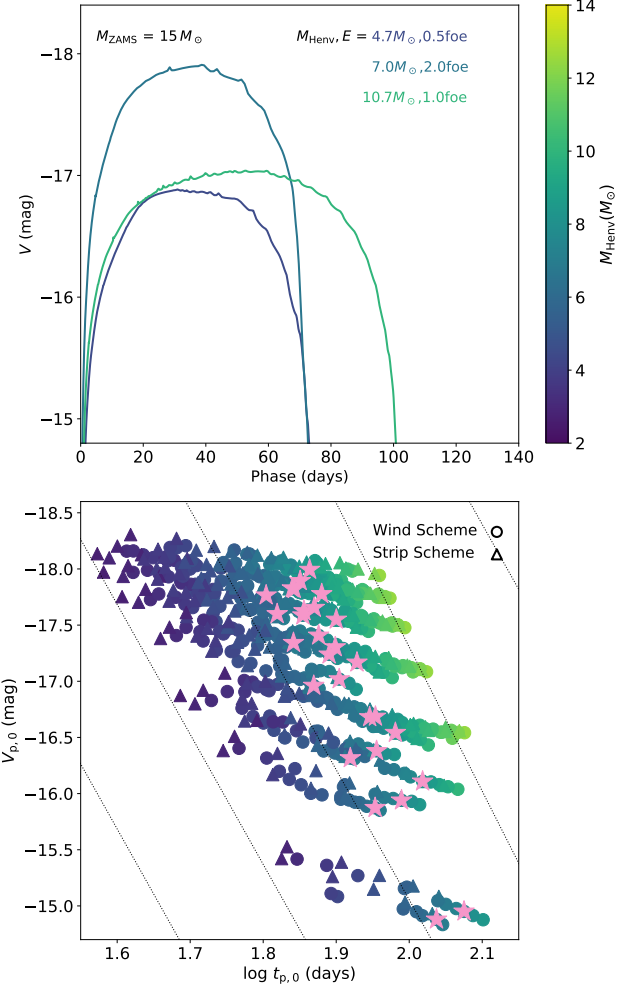


Figure 4. Upper panel: The models with different M_{Henv} , but with light curves adjusted to have the same $t_{p,0}$ or $V_{p,0}$. Lower panel: The relation between $V_{p,0}$ and $t_{p,0}$. The models are color coded by their M_{Henv} , while those generated from progenitors with $\eta=1.0$ (standard wind) are specially labeled by the pink stars.

This quantity is feasible for observation, as $V_{p,0}$ and $t_{p,0}$ can be determined from the observed light curves (while the effect of the ^{56}Ni heating should be corrected for; see §3.4). According to Equation 5, this quantity is determined by both the radius and the mass of the hydrogen-rich envelope, with a much stronger dependence on M_{Henv} than that on R . Figure 5 compares V_{100} with M_{Henv} , where a strong correlation can be immediately discerned ($\rho = -0.98$, $p \ll 0.0001$). M_{Henv} is associated with V_{100} via

$$\frac{M_{\text{Henv}}}{M_{\odot}} = 10^{-0.162 \times V_{100} - 1.703} \quad (8)$$

or

$$V_{100} = -6.17 \times \log \frac{M_{\text{Henv}}}{M_{\odot}} - 10.52, \quad (9)$$

The scatter in Figure 5 is partly attribute to the difference in R . The radii of the progenitor models vary by 0.37 dex, which is equivalent to a difference of 0.07 dex in M_{Henv} given the same V_{100} , according to Equation 5. The 0.07 dex difference is then transformed to a scatter of $\pm 0.6 M_{\odot}$ for $M_{\text{Henv}} = 7.0 M_{\odot}$. Further, for each progenitor model, we have assumed $V_{p,0} \propto \log t_{p,0}^{\alpha}$ in Figure 4. The stretching factor α depends on both M_{Henv} and R , and ranges from 8.10 to 12.84. Fixing it to be 11.65 (Equation 7) will also contribute to the scatter. Usually M_{Henv} and R are not determined priorly from observation, therefore these sources of scatter cannot be reduced. However, the scatter level is relatively small ($< 1 M_{\odot}$ with standard deviation = $0.38 M_{\odot}$; see the lower panel of Figure 5), which in practice can be considered as the random uncertainty when applied to observation, as will be discussed in §4.

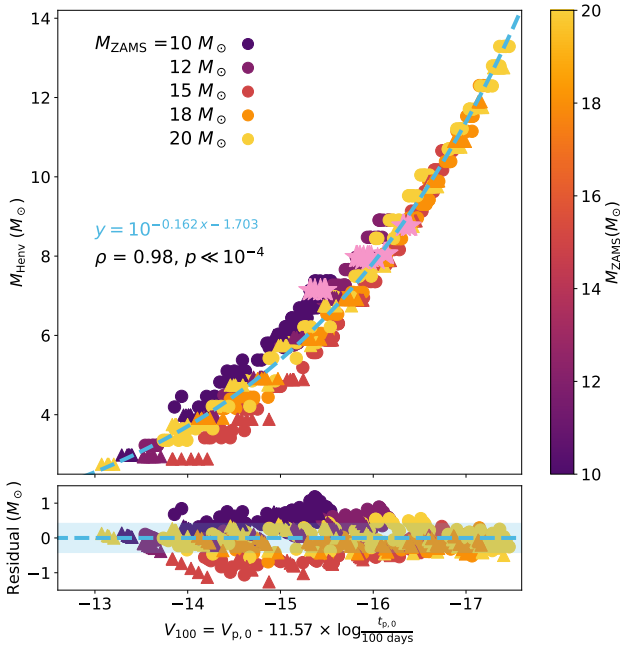


Figure 5. Upper panel: The relation between V_{100} and M_{Henv} . Individual models are color coded by M_{ZAMS} . The dashed line is the best fit. Lower panel: Deviations of each of the models from the fit. The shaded region marks the level of standard deviation.

3.4. Effect of the ^{56}Ni heating

In the previous section, we present a method to measure M_{Henv} for the ^{56}Ni -free model. However, before applying these results to observed SNe II, it is necessary to correct for the effects of the ^{56}Ni heating.

When the photons generated by ^{56}Ni diffuse through the inner ejecta and encounter the recombination front, the propagation of the recombination wave is delayed

due to the continued ionization of the hydrogen-rich envelope by these photons. Observationally, the extra heating from ^{56}Ni extends the plateau duration t_p . The effects of ^{56}Ni on the model with $M_{\text{ZAMS}} = 15 M_{\odot}$, $\eta = 1.0$, $E = 1.0$ foe is shown in the upper panel of Figure 6.

In the literature (see for example Kasen & Woosley 2009; Sukhbold et al. 2016; Goldberg et al. 2019; Kozyreva et al. 2019), the effects of ^{56}Ni on SNe II light curves have been extensively studied. It has been demonstrated that the ^{56}Ni heating has little effect on the magnitude of the plateau, while it significantly extends the plateau duration. The amount of the extension can be estimated as

$$t_p = t_{p,0} \times f_{\text{rad}}^{1/6}, \quad (10)$$

where f_{rad} is the function of M_{Ni} , M_{Henv} , R and E :

$$f_{\text{rad}} = 1 + C_f M_{\text{Ni},1} E_1^{-1/2} R_{500}^{-1} M_{\text{Henv},10}^{-1/2}. \quad (11)$$

Here, $M_{\text{Ni},1}$, R_{500} , $M_{\text{Henv},10}$ and E_1 are M_{Ni} , R , M_{Henv} and E in the units of $1 M_{\odot}$, $500 R_{\odot}$, $10 M_{\odot}$ and 1 foe, and C_f is the normalized constant that depends on the model grid (Kasen & Woosley 2009; Sukhbold et al. 2016; Goldberg et al. 2019).

In Sukhbold et al. 2016 and Goldberg et al. 2019, the effect of Ni-heating is investigated in a relatively narrow range of $f_{\text{rad}} = 1.00 - 1.15$, while the model grid in this work encompasses a largely expanded parameter space, and f_{rad} ranges from 1.00 to 1.70. Applying Equation 11 to the models with $f_{\text{rad}} < 1.15$, we derive $C_f = 52$, as shown in the lower panel of Figure 6. For comparison, the result from Goldberg et al. (2019), where $C_f = 87$, is also plotted. The result in this work is more consistent with that from Sukhbold et al. (2016) where $C_f = 50$. However, unlike the results in previous works, we find that a single value of C_f can not provide reasonably good fit for all the models. When f_{rad} increases to > 1.2 , we find significant deviations, where the fit to these models returns $C_f = 97$. The difference in C_f is not surprising: indeed, the models with $f_{\text{rad}} > 1.2$ are large in M_{Ni} but low in E and M_{Henv} . The amount of radioactive energy, which is proportional to M_{Ni} , dominates over internal energy at recombination, which scales as E . The recombination is therefore more affected than models that radioactive energy and internal energy are comparable ($f_{\text{rad}} \leq 1.2$), which is reflected in the increase in C_f .

Similar to Goldberg et al. (2019), where the scaling relation connecting t_p with M_{Ni} , M_{Henv} , E , and R was suggested for ^{56}Ni -rich events, we perform a power-law

fit to the models with $M_{\text{Ni}} \geq 0.04 M_{\odot}$, and find

$$\log \frac{t_p}{\text{days}} = 2.31 + 0.20 \log M_{\text{Ni},1} + 0.54 \log M_{\text{Henv},10} - 0.30 \log E_1 - 0.06 \log R_{500}. \quad (12)$$

The coefficients are in good agreement with those in Goldberg et al. (2019).

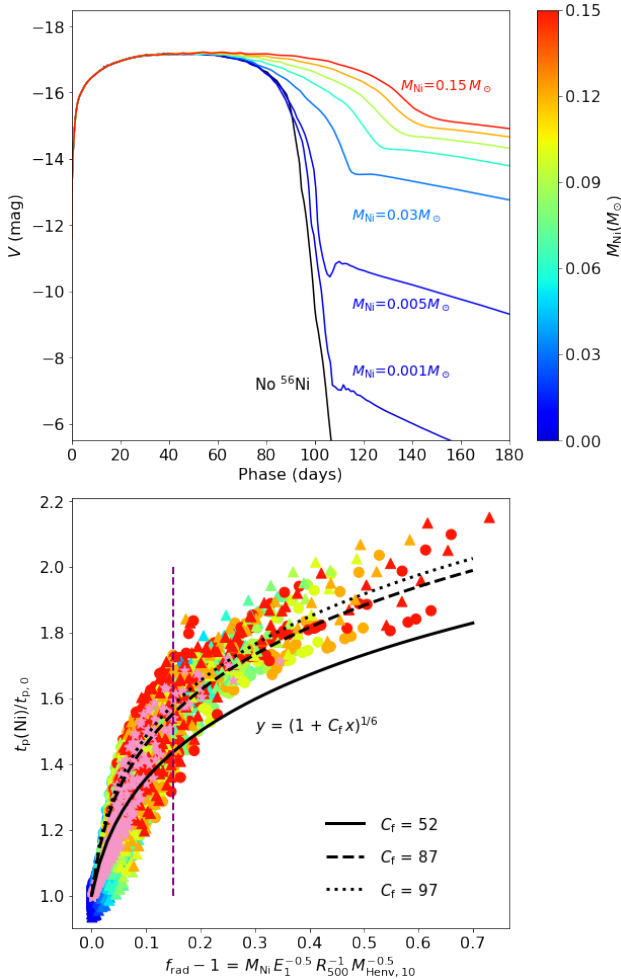


Figure 6. Upper panel: The V-band light curve of the model with $M_{\text{ZAMS}} = 15 M_{\odot}$, $\eta = 1.0$ and $E = 1$ foe, but with different M_{Ni} , as color coded by the colorbar. Lower panel: Plateau duration of models with ^{56}Ni divided by the plateau duration for the nickel-free models, and are compared to the scaling Equation 11 with different values of C_f . The meaning of the markers are the same as Figure 3. The models with $\eta = 1.0$ are specially labeled by the pink stars. The purple vertical line roughly marks the upper limit of the parameter space of previous model surveys (Sukhbold et al. 2016; Goldberg et al. 2019)

Although Equations 11 and 12 provide useful ways to estimate the effect of ^{56}Ni on the duration of the SNe

II light curve once M_{Ni} , E , M_{Henv} and R are determined, in practice, we are always facing with the inverse problem, i.e., extracting these information from the light curves. It is therefore important to establish a method to estimate the effects of the ^{56}Ni heating from observables rather than the physical properties of the explosion.

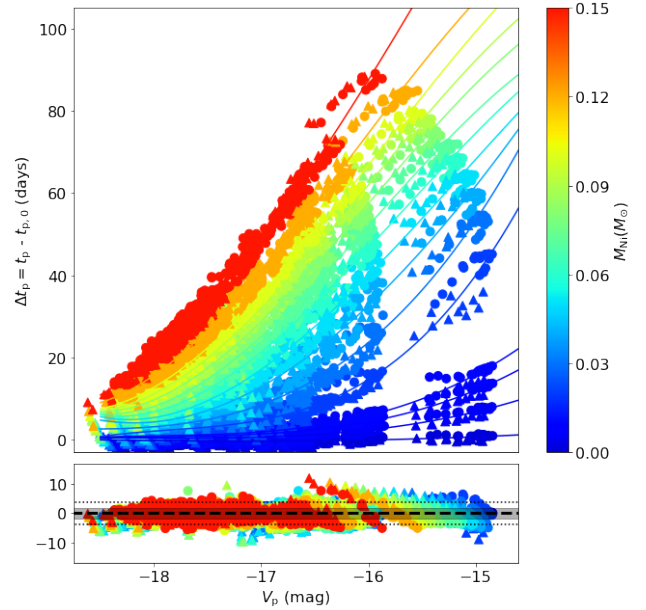


Figure 7. Upper panel: The comparison between the amount of plateau extension Δt_p and the plateau magnitude V_p . Models with different ^{56}Ni mass are color coded by the color bar. The third-degree polynomial fits are shown by the solid lines. The meaning of the markers are the same as Figure 3. Lower panel: The residuals of the third-degree polynomial fits. The shaded region represents the standard deviation (1.75 days). The dotted lines represent the 95% CI (3.70 days).

From Equation 11, for the fixed M_{Ni} , the plateau duration of models with low explosion energy E , small radius R and small hydrogen-rich envelope mass M_{Henv} tend to be more extended. As indicated by Equation 5, decreases in E and R lead to low luminosity events. However, low M_{Henv} is associated with a bright and short plateau. In this case, although $t_p/t_{p,0}$ can be large, the actual difference $t_p - t_{p,0} = t_{p,0} \times (t_p/t_{p,0} - 1)$ may be small (because $t_{p,0}$ is small). Motivated by the above discussion, in Figure 7, the plateau magnitude V_p is compared with the extension of the plateau duration, $\Delta t_p \equiv t_p - t_{p,0}$. We find an important feature, i.e., once M_{Ni} is fixed, the difference in the plateau duration Δt_p is primarily determined by V_p , and bright events tend to be more extended. The relation between Δt_p

$M_{\text{Ni}} (M_{\odot})$	A	B	C	D
1×10^{-3}	0.002	0.014	-0.028	-0.021
5×10^{-3}	0.020	0.012	-0.008	0.041
8×10^{-3}	0.041	-0.013	0.047	0.066
0.01	0.049	0.001	0.046	0.094
0.02	0.140	-0.064	0.195	0.208
0.03	0.080	0.246	0.211	0.315
0.04	-0.030	0.644	0.244	0.432
0.05	-0.099	0.856	0.413	0.538
0.06	-0.134	0.940	0.649	0.677
0.07	-0.158	0.977	0.872	0.812
0.08	-0.156	0.953	1.103	0.971
0.09	-0.150	0.910	1.318	1.116
0.10	-0.135	0.856	1.525	1.276
0.12	-0.158	0.879	1.810	1.569
0.15	-0.073	0.7094	2.233	2.020

Table 2. Polynomial coefficients of Equation 13.

and V_p is approximated by third-degree polynomial as

$$\frac{\Delta t_p}{10 \text{ days}} = A \times (V_p + 18)^3 + B \times (V_p + 18)^2 + C \times (V_p + 18) + D, \quad (13)$$

where the coefficients A, B, C, D depend on M_{Ni} , and are listed in Table 2. The standard deviation of the residuals is 1.75 days, as shown by the shaded region in the lower panel of Figure 7, and the 95% confidence interval (CI) is defined by ± 3.70 days. We note here that Equation 13 is only applicable for the range of V_p shown in Figure 7.

Unlike Equations 11 and 12, the correction of t_p for the effects of ^{56}Ni heating, using Equation 13, is derived empirically based on observables. This correction therefore does not require any prior knowledge on the physical properties of the explosion, except for M_{Ni} , which can be independently and robustly measured from the radioactive tail of the light curve (Woosley 1988; Arnett & Fu 1989; Hamuy 2003; Spiro et al. 2014; Anderson 2019; Rodríguez et al. 2021) or roughly estimated from the plateau magnitude (Hamuy 2003; Kasen & Woosley 2009; Valenti et al. 2016; see also §4).

4. APPLICATION TO OBSERVATION

In the previous section, we have shown that the plateau phase of SNe II light curve does not provide substantial information about M_{ZAMS} of the progenitor, while the combination of the plateau magnitude and

duration can constrain the envelope mass M_{Henv} within an uncertainty of $1 M_{\odot}$. In this section, the analytical results are applied to the observed SNe II sample to establish the distribution of M_{Henv} , which is employed to emphasize the uncertainty associated with the pre-SN mass-loss mechanism.

In this work, we collect light-curve data of normal SNe II from the literature that have dense V -band photometric observations. The primary sources are Anderson et al. (2014) and Valenti et al. (2016), complemented by other well observed individual objects (Table A1). The inclusion criterion is the availability of V -band photometry that cover both the plateau phase and the transition from the plateau to the linear decay tail, which enables the measurement of t_p . The final sample consists of 99 normal SNe II.

To measure the plateau duration t_p , we fit the V -band light curve around the drop from the plateau with Equation 3, using the python routine `scipy.optimize.curve_fit`. The main source of the uncertainty comes from the uncertainty of the explosion date, and the typical value is 5 to 10 days. It is important to note that the measurements of t_p for the models and the observation data are different, as for the observed light curve, the maximum magnitude on the plateau is usually not well-determined. Our experiment on fitting the nickel-rich model light curves with Equation 3 reveals a systematic offset between the plateau duration measured in §3.1 (hereafter denoted as t_p), and the ones derived from Equation 3 fitting (hereafter denoted as $t_{p,\text{fit}}$)

$$t_{p,\text{fit}} = t_p + 6.6 \text{ days}. \quad (14)$$

For the observed SNe II, the plateau duration are corrected by Equation 14, and the standard deviation of the residual, which is 5 days, is included in the uncertainties of the measurements. Once t_p is determined, the plateau magnitude is measured by the interpolation of the observed light curve at $0.5 \times t_p$. The main uncertainty of V_p comes from the uncertainty of the estimations of distance and extinction.

A correlation between the plateau magnitude and the ^{56}Ni mass was firstly reported by Hamuy (2003), and confirmed by many subsequent works (Kasen & Woosley 2009; Valenti et al. 2016). Among the 99 SNe II in our sample, 79 of them have well constrained M_{Ni} , and they are connected with V_p through

$$\log \frac{M_{\text{Ni}}}{M_{\odot}} = -0.385 \times V_p - 7.851, \quad (15)$$

as shown in the upper panel of Figure 8. The standard deviation of the residual is 0.24 dex. For objects with-

out independent measurement on the radiative tail, their M_{Ni} are determined by Equation 15. The uncertainty of V_p is propagated to that of M_{Ni} .

After determining t_p and M_{Ni} , the extension of plateau by the ^{56}Ni heating, Δt_p , is corrected through Equation 13. We use Monte Carlo techniques to estimate the uncertainty. For each object, We perform 1000 simulations. In each trial, the uncertainty of V_p is randomly assigned assuming Gaussian distribution. Because M_{Ni} is estimated from the luminosity of the tail or the plateau magnitude, the uncertainties of which mainly come from the distance and extinction estimations, so we assume $\sigma \log M_{\text{Ni}} = 0.4 \times \sigma V_p$ and randomly assigned to $\log M_{\text{Ni}}$. Here $\sigma \log M_{\text{Ni}}$ and σV_p are the uncertainties of $\log M_{\text{Ni}}$ and V_p . With V_p and M_{Ni} kept fixed, the plateau duration extended by the ^{56}Ni heating, Δt_p , is derived from Equation 13. The uncertainty of Δt_p is the standard deviation of the 1000 measurements. The plateau duration without the ^{56}Ni heating, $t_{p,0}$, is then determined. Here we do not attempt to correct the effect of ^{56}Ni heating on plateau magnitude V_p because such effect is significant only when the plateau is faint but M_{Ni} is large, which is not seen in observation (Equation 15). For convenience, in the following text, we simply assume $V_p = V_{p,0}$. The comparison of $\log t_{p,0}$ and $V_{p,0}$ is shown in the lower panel of Figure 8.

Two interesting features can immediately be discerned: (1) the observed SNe II cover a much broader range than that predicted by the standard stellar wind models ($\eta = 1.0$; the pink strip) in the $\log t_{p,0} - V_p$ diagram; (2) most SNe II have E less than 1.0 foe (the light blue strip). The diversity in plateau duration and magnitude of SNe II, as well as the lack of correlation, has also been reported by Anderson et al. (2014). However, in their work, the plateau duration is not corrected for the effect of the ^{56}Ni heating, and the magnitude is defined at the maximum light of the initial peak. Although the uncertainty is relatively large, we find that the range of the observed SNe II in the $\log t_{p,0} - V_{p,0}$ diagram can be fully accounted for by the models in this work, with M_{env} ranging from 3 to $14 M_{\odot}$. The mean value of M_{Henv} is $6.75 M_{\odot}$, and the standard deviation is $2.98 M_{\odot}$.

Assuming M_{Henv} measured for the SNe II sample represents what is found in nature, we can examine whether its distribution matches with the one expected by the mass-loss driven by stellar wind. For this purpose, we need to establish the relation between M_{ZAMS} and M_{Henv} . We employ 3 progenitor model grids: (1) the fiducial model described in §2.1; (2) strong overshoot model, identical to the fiducial model except for the enhanced overshooting parameter $f_{\text{ov}} = 0.025$; (3) the grid

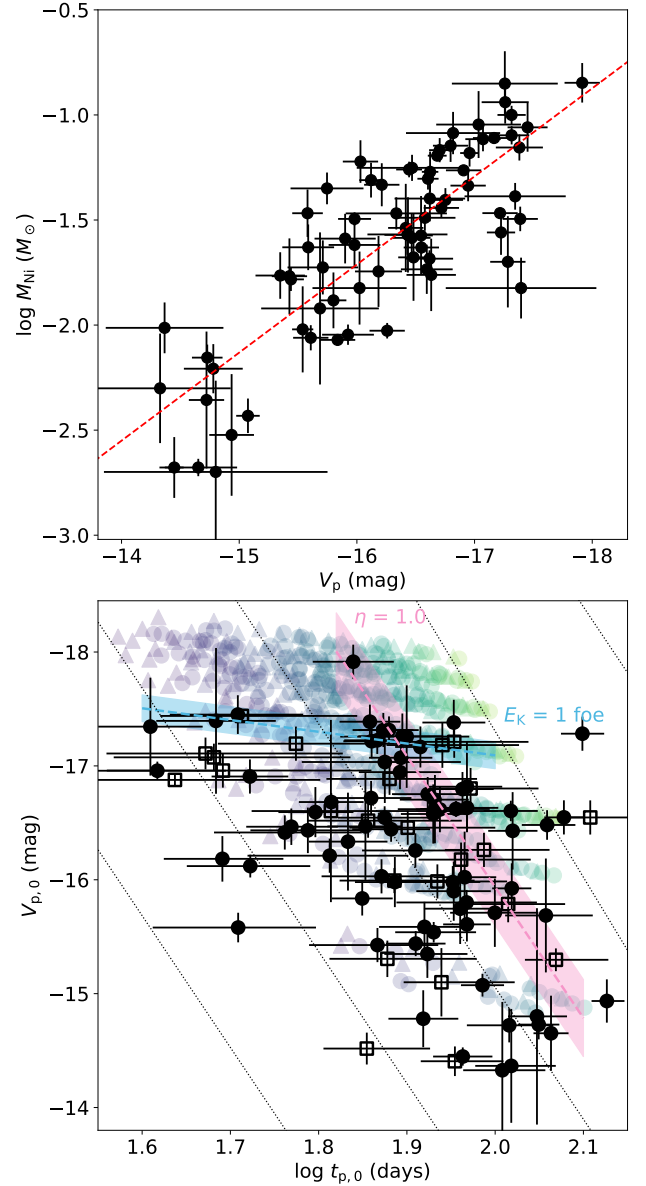


Figure 8. Upper panel: The relation between plateau magnitudes V_p and the ^{56}Ni masses M_{Ni} of SNe II with well constrained M_{Ni} from the radiative tail ($N = 79$). The red dashed line is the linear regression to the data (Equation 15). Lower panel: The comparison of the plateau magnitudes and the plateau duration, corrected for ^{56}Ni heating, of the SNe II sample in this work ($N = 99$). Objects with and without well constrained M_{Ni} are labeled by the black dots and open squares respectively. The light blue strip indicates the range of models with $E = 1$ foe, while the pink strip indicates the models with wind efficiency $\eta = 1.0$ (standard stellar wind).

calculated by Kepler (Sukhbold et al. 2016). For model grids (1) and (2), we assume $\eta = 1.0$, and M_{ZAMS} ranges from 10 to $20 M_{\odot}$ with $0.5 M_{\odot}$ increments. The relations between M_{ZAMS} and M_{Henv} of these models are shown in the upper panel of Figure 9.

For the fiducial models, the increase in M_{ZAMS} leads to more massive hydrogen-rich envelope if $\eta = 0.0$, while at the same time, the wind mass-loss also becomes more significant. The final M_{Henv} is restricted to a relatively narrow range as a result of the competition between these two factors, which is similar to the $M_{\text{ZAMS}}-M_{\text{Henv}}$ relation of the `Kepler` model grid. Compared with the fiducial models, the strong overshoot models possess more massive and luminous helium cores for fixed M_{ZAMS} , and are more efficient in the wind mass-loss. When M_{ZAMS} reaches to $15 M_{\odot}$, the aforementioned balance is disrupted, and M_{Henv} rapidly decreases down to $\sim 3 M_{\odot}$ following the continue increase of M_{ZAMS} .

We first calculate the distributions of M_{Henv} expected by these theoretical models. The distribution of M_{ZAMS} is empirically characterized by the initial mass function. In this work, we employ the Salpeter form (Salpeter 1955)

$$\frac{dN}{dM_{\text{ZAMS}}} \propto M_{\text{ZAMS}}^{-2.35}. \quad (16)$$

Using Monte Carlo techniques, a large sample ($N = 10^4$) of progenitors with M_{ZAMS} ranging from 10 to $20 M_{\odot}$ is generated, following the distribution described by Equation 16. For each progenitor, we calculate its M_{Henv} from the $M_{\text{ZAMS}}-M_{\text{Henv}}$ relations illustrated in the upper panel of Figure 9. The resulting distributions of M_{Henv} for the different progenitor grids are shown in the lower panel of Figure 9.

The most significant difference between the observations and the theoretical models lies in the range of M_{Henv} . An unusually large fraction ($\sim 60\%$) of SNe II are found to have M_{Henv} lower than $6.8 M_{\odot}$, the lower bound of the fiducial and `Kepler` models. While the strong overshoot models roughly match the lower end of the observed distribution, more than 30% of SNe II possess M_{Henv} larger than the $7.2 M_{\odot}$ upper bound predicted by these models. None of the progenitor model types can explain the M_{Henv} distribution of the SNe II sample.

The failure to reproduce the observed M_{Henv} distribution prompts us to reconsider the strong assumptions we have made in this study: (1) standard stellar wind ($\eta = 1.0$), and (2) single-star evolution. Indeed, these two assumptions are not very solid. Regarding the assumption (1), the RSG mass-loss rate is not tightly constrained from observation. Factors such as wind clumping can enhance the mass-loss rate, while it is not included in the `Dutch` scheme of `MESA`. As demonstrated by the strong overshoot models, the change in the microphysics in the progenitor can significantly affect the mass loss. For the fiducial models, we have assumed the identical convection scheme, while the convection pro-

cess and overshooting can depend on M_{ZAMS} , or vary on a case-by-case basis. The absence of a robust theory on convection contributes to the uncertainty in the mass-loss rate. Further, we have assumed non-rotating progenitor models without magnetic field, despite the significant effects these factors can have on the mass-loss rate. While these uncertainties are absorbed in the freely-adjusted η in this study, self-consistent modeling that includes all these factors is required to examine whether the M_{Henv} distribution of SNe II is physically plausible if the hydrogen-rich envelope is solely stripped by single star evolution. Aside from the wind mass-loss rate, the pre-SN mass-loss channel represents another source of uncertainty. Accumulating evidences suggest that binary interaction plays a crucial role in stripping mass from the progenitor prior to the explosion (see references in §1). Depending on the mass ratio of the primary/secondary star and the orbit separation, the hydrogen-rich envelope can either be fully stripped or retained. The wide range of M_{Henv} of SNe II can, therefore, be covered by varying orbital parameters of the binary scenario.

The M_{Henv} distribution derived in this work is very useful to constrain the nature of CCSNe progenitors. In §3.1, we have shown that the light curves of SNe II provide limited information regarding the M_{ZAMS} of the progenitor. Measuring M_{ZAMS} from SNe II light curves therefore heavily relies on the correlation between $M_{\text{ZAMS}}-M_{\text{Henv}}$ when strong assumptions on the stellar wind are made. This study shows that the models based on these assumptions indeed fail to produce the observation. Modified mass-loss rate for a single star, or binary interaction, are needed to explain the M_{Henv} distribution of SNe II. However, the current study does not allow us to conclude which factor is the dominant, or whether they all contribute equally to differ the observed M_{Henv} from the predictions of single star models evolving with the standard stellar wind. Further, the SNe II sample in this work is collected from the literature with various observational sources, making it difficult to estimate the possible observational biases. In the future survey, large, homogeneous sample of SNe II light curves is required to derive the representative distribution of M_{Henv} to better constrain the mass-loss mechanism of CCSNe.

5. DISCUSSION

5.1. Comparison with SNEC

In §3, we calculate the V -band light curves of a grid of progenitors, with different M_{ZAMS} , mass-loss rates, and energy E , using the one-dimensional multi-frequency radiation hydrodynamics code `STELLA`. Except for `STELLA`, the SuperNova Explosion Code (`SNEC`; Morozova et al.

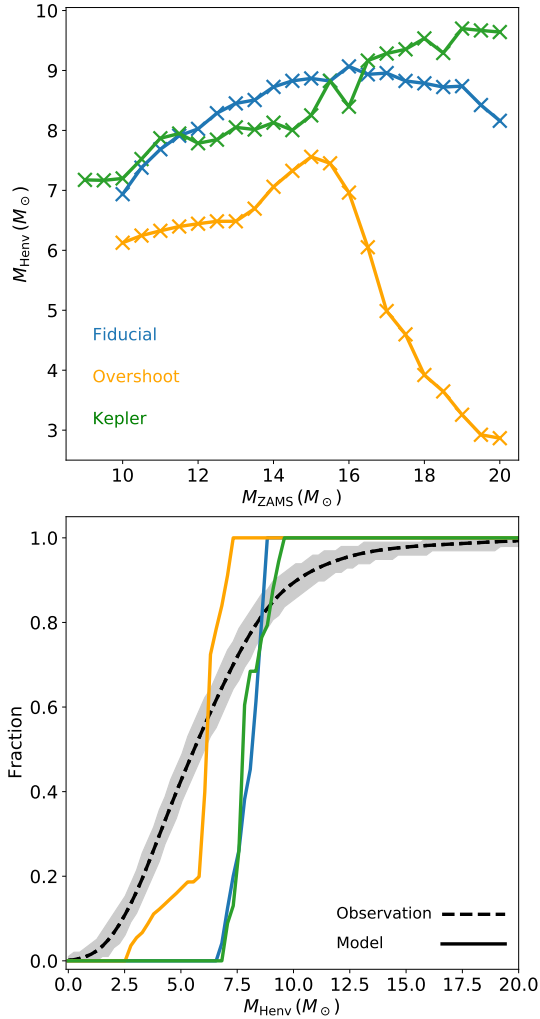


Figure 9. Upper panel: The relation between M_{ZAMS} and M_{HeIV} predicted by the progenitor models. Blue: fiducial models; orange: strong overshoot models; green: models from kepler; Lower panel: The distributions of M_{HeIV} . The black dashed line is for the observed SNe II sample, and the shaded region marks the 95% CI. The color lines are the predictions of the progenitor models.

2015) is also another open-source radiation hydrodynamic code for core-collapse SNe which is frequently employed in the literature to constrain the progenitor parameters. Unlike STELLA which uses a multi-group approach to radiation transfer, SNEC employs a simplified opacity floor approximation while utilizing the complete OPAL opacity tables. The differences in the opacity can strongly affect the light curve. It is therefore important to compare the outputs from the two codes to investigate the effects of the treatment for the radiative transfer, and test the robustness of the results presented in §3.

We employ the same progenitor model grid described in §2.1, evolved to the core carbon depletion, as the input of SNEC. The energy is manually deposited in the inner $0.2 M_{\odot}$ of the progenitor models, using the thermal bomb mode, to trigger the explosions. We use the same setup, including the mass-cut and the mixing scheme, as outlined in §2.2. No ^{56}Ni is introduced into the simulations of SNEC.

The V-band light curves generated by SNEC and STELLA for the typical progenitor models are shown in Figure 10. Overall, we find general consistency between the two codes. However, while the light curves generated by STELLA appear to be flat and the maximums are usually reached at the mid point of the plateau, the light curves generated by SNEC have distinct feature: they reach their maximums shortly after the explosions, and then gradually fade. As a result, although the light curves from SNEC and STELLA have similar maximum magnitudes, the plateau magnitudes, which are measured at $0.5 \times t_{p,0}$ by definition, differ. Depending on the progenitor parameter, $V_{p,0}$ of SNEC light curves can be ~ 0.5 mag fainter than those measured from STELLA light curves.

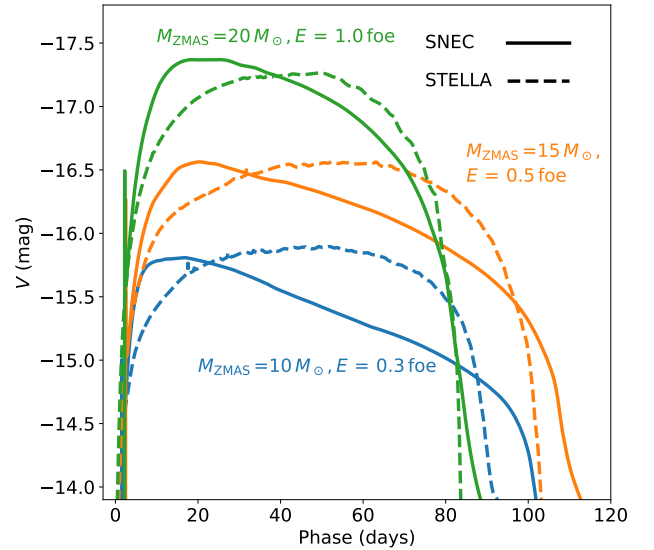


Figure 10. The comparison between light curves generated by SNEC (solid lines) and STELLA (dashed lines) for progenitors with $\eta = 1.0$.

Neglecting the shapes of the light curves, we compare $V_{p,0}$ and $t_{p,0}$ measured for SNEC and STELLA, which are shown in Figure 11. The linear regressions return

$$\begin{aligned} V_{p,0}^{\text{SNEC}} &= 1.22 \times V_{p,0}^{\text{STELLA}} + 3.78 \\ \log \frac{t_{p,0}^{\text{SNEC}}}{\text{days}} &= 1.15 \times \log \frac{t_{p,0}^{\text{STELLA}}}{\text{days}} - 0.30. \end{aligned} \quad (17)$$

When the plateau is short and faint, the deviations of both $V_{p,0}$ and $t_{p,0}$ are relatively large. This is consistent with Figure 10. By fitting $V_{p,0}$ and $t_{p,0}$ of SNEC light curves with M_{Henv} , R and E , we derive the scaling relations

$$\begin{aligned} V_{p,0} &\sim -2.02 \log R + 1.80 \log M_{\text{Henv}} - 2.32 \log E \\ \log t_{p,0} &\sim -0.06 \log R + 0.63 \log M_{\text{Henv}} - 0.21 \log E. \end{aligned} \quad (18)$$

The standard deviations of the residuals to the fits are 0.05 mag (for $V_{p,0}$) and 0.01 dex (for $t_{p,0}$) respectively. We find for $t_{p,0}$, the scaling relation is similar to Equation 5, and again confirm the weak dependence of $t_{p,0}$ on R . However, compared with STELLA, $V_{p,0}$ measured for SNEC show stronger dependencies on all the physical parameters.

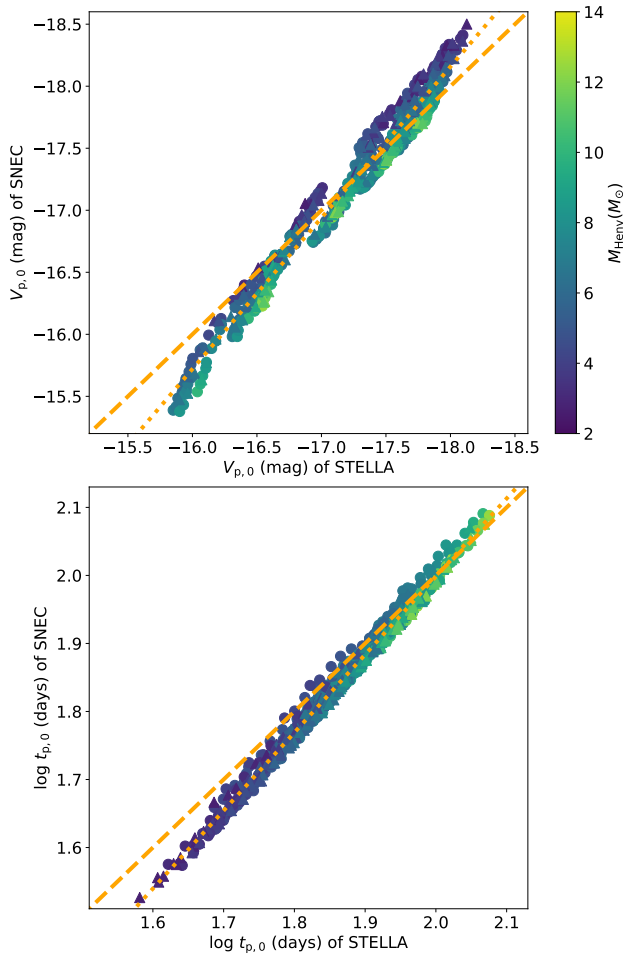


Figure 11. The comparison between $V_{p,0}$ (Upper panel) and $t_{p,0}$ (Lower panel) of light curves generated by SNEC and STELLA. The dashed lines are one-to-one correspondence, and the dotted lines are the linear regressions. Models are color coded by M_{Henv} .

The investigation on the possible reasons for the differences between the outputs of SNEC and STELLA is beyond the scope of this work. Instead, we are more interested in how the results in this work are affected. Similar to the practice in §3, by eliminating E in Equation 18, we derive

$$V_{p,0} - 10.75 \log t_{p,0} \sim -1.24 \log R - 5.07 \log M \quad (19)$$

Motivated by Equation 19, we define for SNEC

$$V_{100}^{\text{SNEC}} = V_{p,0} - 10.75 \times \log \frac{t_{p,0}}{100 \text{ days}}, \quad (20)$$

which is then compared with M_{Henv} in Figure 12. Similar to the discussion in §3.3, we find a strong correlation between V_{100}^{SNEC} and M_{Henv} ($\rho = -0.98$, $p \ll 0.0001$). The two quantities are connected via

$$\frac{M_{\text{Henv}}}{M_{\odot}} = 10^{-0.173 \times V_{100}^{\text{SNEC}} - 1.846} \quad (21)$$

or

$$V_{100}^{\text{SNEC}} = -5.780 \times \log \frac{M_{\text{Henv}}}{M_{\odot}} - 10.670. \quad (22)$$

The standard deviation of the residuals from the fit is $0.455 M_{\odot}$. Compared with the result from STELLA (the light blue dashed line in Figure 12), Equation 8 overestimates M_{Henv} in the range of V_{100}^{SNEC} considered in this work (-13 to -18 mag), with the maximum deviation of $\sim 10\%$. The consistency between the results of the two codes, i.e., STELLA and SNEC, suggests that using V_{100} as the indicator of M_{Henv} is robust against the different treatments for the radiative transfer.

5.2. The moment when the explosion is launched

In this work, the progenitors are evolved to the moment when carbon in the core is exhausted, and the energy is subsequently deposited to trigger the explosion. This simplification allows us to calculate the light curves of progenitor models with M_{ZAMS} down to $10 M_{\odot}$, which, in our own experiments with MESA, develop strong shell-burning and off-center flames, and hardly progress to core-collapses. Our goal here is to investigate whether this simplification would affect the properties of the light curve.

The upper panel of Figure 13 shows the evolutionary track of the progenitor model with $M_{\text{ZAMS}} = 15 M_{\odot}$ and $\eta = 1.0$ on the Hertzsprung-Russel diagram (HRD). As illustrated in the middle panel of Figure 13, most of the hydrogen-rich envelope is stripped before the carbon burning phase. About 10^4 years after the ignition of carbon, the core starts to collapse. The mass-loss rate during this period is about $10^{-6} M_{\odot} \text{ yr}^{-1}$, therefore

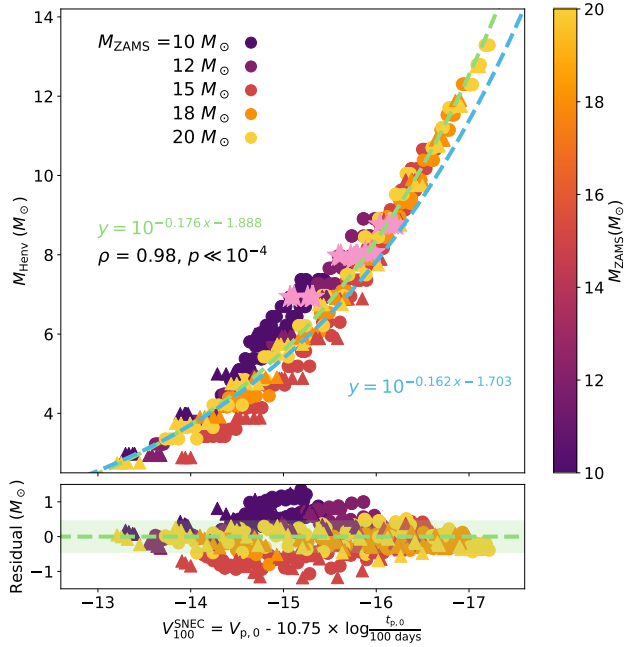


Figure 12. Upper panel: The relation between V_{100}^{SNEC} and M_{HeNV} . Individual models are color coded by M_{ZAMS} , while those with $\eta = 1.0$ are specially labeled by the pink stars. The green dashed line is the best fit. The best fit for the models of STELLA (Figure 5) is plotted by the light blue dashed line for comparison. Lower panel: Deviations of each of the models from the fit. The shaded region marks the level of standard deviation.

M_{HeNV} only changes by about $0.01 M_{\odot}$, which is negligible in practice. The evolution of stellar radius is more complicated. In response to core helium burning, the star expands, ejecting the loosely-bounded hydrogen-rich envelope. The radius reaches its local maximum ($\sim 600 R_{\odot}$) when helium in the core is exhausted. After then, the radius decreases due to substantial mass-loss. The star expands again following the shell helium burning and core carbon ignition, and settles at the (almost) constant radius after core carbon depletion.

We employ two additional stellar structures, one taken at the core oxygen depletion and the other at the moment of the core-collapse, as the inputs of STELLA. The explosions are triggered following the procedure described in §2.2, and the resulting V -band light curves are compared with the fiducial models in this work, as shown in Figure 14. We find that the light curves are almost identical once E is fixed. This is not surprising, considering that the two main physical parameters governing the light curve properties, i.e., M_{HeNV} and R , hardly evolve after the core carbon depletion.

5.3. Velocity as an independent constraint

In this work, we have developed a method to constrain the hydrogen-rich envelope mass of the progenitor from the light curve of SNe II. One of the main advantages of this technique is its reliance solely on photometry, and does not require information from the spectroscopy that is not always available especially for faint events. In this section, we briefly discuss whether the photospheric velocity, inferred from the minimum of the absorption features emerged in the plateau phase spectra, can provide additional constraints on M_{ZAMS} of the progenitor.

As discussed in the previous sections, the properties of the light curve at the plateau phase are primarily determined by the hydrogen-rich envelope. Given the same explosion energy, models with different M_{ZAMS} but the same M_{HeNV} will generate very similar light curves. Although in this work, M_{HeNV} is arbitrarily adjusted to mimic the diverse mass-loss channels (see discussion in §4), the mass of the helium core $M_{\text{He,core}}$ is insensitive to the remaining envelope and is almost uniquely determined by M_{ZAMS} . Models with the same M_{HeNV} , being indistinguishable from the light curve, can be diverse in the ejecta mass M_{eje} . Such difference is expected to manifest itself in the photospheric velocity v_{ph} , which is associated with the explosion energy via

$$E \sim \frac{1}{2} M_{\text{eje}} v_{\text{ph}}^2, \quad (23)$$

The evolution of photospheric velocities for some typical models are shown in Figure 15. Here, the photosphere is defined by Sobolev opacity $\tau_{\text{Sob}} = 2/3$. We select two progenitor sets, one with $M_{\text{HeNV}} = 7.0 M_{\odot}$, the average value of the observed SNe II sample (see §4), and the other with $M_{\text{HeNV}} = 3.0 M_{\odot}$. For the latter case, the variation in M_{eje} is the most pronounced, ranging from $4.4 M_{\odot}$ to $7.5 M_{\odot}$. Consistent with the findings of Goldberg et al. (2019), the difference in M_{eje} is reflected in v_{ph} before 20 days after the shock breakout, despite these models have the same M_{HeNV} . However, it is important to note that the photospheric velocity measured at early phase is highly sensitive to the outermost density structure of the hydrogen-rich envelope, and can be significantly affected by the presence of CSM (see for example Figure 2 of Moriya et al. 2023), which is not included in the current model grid. We defer the detailed investigation on the effects of CSM on both the photospheric velocity and the light curve to future work.

At ~ 30 days after the explosion, the photosphere cools down to ~ 6000 to 7000 K, which is set by the temperature when the recombination of hydrogen occurs. The recession of the photosphere slows down following the development of the hydrogen recombination, and the models with the same M_{HeNV} settle down at the similar v_{ph} . Although there are still some variations, not

much can be said as these variations are relatively small and are not monotonic functions of M_{ZAMS} .

We now seek for the scaling relations between v_{ph} and other observables or physical properties. The correlation between the photospheric velocity and the luminosity of the light curve, measured at ~ 50 days after the explosion, is firstly discovered by Hamuy (2003), based on a sample of nearby SNe II. The physics of this correlation is then explained by Kasen & Woosley (2009). The luminosity, assuming black-body radiation, can be expressed as

$$L \approx 4\pi\sigma R_{\text{ph}}^2 T_{\text{ph}}^4. \quad (24)$$

At the plateau phase, the dynamics of the ejecta can be well characterized by the homologous expansion, i.e., $v(R, t) = R/t$ (Goldberg et al. 2019), and the temperature of the photosphere remains relatively constant at $T_{\text{ph}} \approx 6000$ K, set by the hydrogen recombination, although observations indicates certain degree of variation (Valenti et al. 2016). At the given phase t , say, 50 days after the explosion, the photospheric velocity is correlated with luminosity through $L_{50} \propto v_{\text{ph},50}^2$. For the model grid in this work, it is difficult to determine the phase at which the photospheric velocity should be measured. Some light curves in this work have plateau duration shorter than 40 days. Similar to the plateau magnitude, we measure the photospheric velocity $v_{\text{ph},0}$ at $0.5 \times t_{\text{p},0}$ for the 636 ^{56}Ni -free models in the grid, and we find

$$\begin{aligned} V_{\text{p},0} = & -4.84 \log \frac{v_{\text{ph},0}}{10^3 \text{ km s}^{-1}} \\ & -3.75 \log \frac{t_{\text{p},0}}{100 \text{ days}} - 14.17. \end{aligned} \quad (25)$$

The standard deviation of the residual to the fit is 0.07 mag. By fixing $t_{\text{p},0}$ to ensure that the photospheric velocities are all measured at the same phase, we derive $V_{\text{p},0} \propto -4.84 \log v_{\text{ph},0}$, or $L_{\text{p},0} \propto v_{\text{ph},0}^{1.94}$, which is in good agreement with the above analysis. The photospheric velocity is connected to the physical properties via

$$\log v_{\text{ph},0} \sim 0.11 \log R - 0.58 \log M_{\text{Henv}} + 0.55 \log E, \quad (26)$$

which confirms the degeneracy proposed by Goldberg et al. (2019) and Goldberg & Bildsten (2020): Equation 26 is essentially a linear combination of Equation 4 through Equation 25, and it does not contain any additional information regarding R , M_{Henv} and E .

6. CONCLUSION

In this work, we investigate the V -band light curve characteristics of SNe II, using a grid of progenitor models with various ZAMS masses, hydrogen-rich envelope

masses, ^{56}Ni masses and explosion energies calculated by MESA + STELLA. To account for the uncertainties in the pre-SN mass-loss channels and mass-loss rates, the hydrogen-rich envelope is manually removed at the moment of the core helium depletion. We find that models with the same envelope mass and explosion energy exhibit similar light curves, even though their M_{ZAMS} are different. Inferring M_{ZAMS} from light curve modeling therefore can be very uncertain if the mass-loss history is not known in prior. This degeneracy, originally proposed by Dessart & Hillier (2019), is extended in this work to encompass the typical range of the envelope masses of SNe II.

Additionally, we establish the scaling relation between the light curve characteristics and the envelope mass M_{Henv} , radius R and explosion energy E for the ^{56}Ni -free models. We find a scaling relation for the plateau magnitude $V_{\text{p},0}$ that is very similar with previous studies (see Popov 1993; Kasen & Woosley 2009; Sukhbold et al. 2016; Goldberg et al. 2019 for examples). However, the dependence of plateau duration $t_{\text{p},0}$ on R is surprisingly weak, as shown in our Figure 3, contrary to the proposed scaling $t_{\text{p},0} \propto R^{1/6}$. Based on these equations, we develop a method to measure M_{Henv} by combining $V_{\text{p},0}$ and $t_{\text{p},0}$. We find M_{Henv} can be well constrained within an uncertainty of $1 M_{\odot}$ (Figure 5). The effects of the ^{56}Ni heating, known to potentially extend the plateau duration, are also thoroughly discussed in this study. We find that once the mass of ^{56}Ni is fixed, the amount of plateau extension is almost uniquely determined by the plateau magnitude V_{p} . Considering that M_{Ni} can be robustly inferred from the radioactive tail based on the assumption of full γ -ray trapping at the nebular phase, our results provide an approach to quantify the effects of the ^{56}Ni heating from observables.

To ensure the robustness of our results, we employ the same progenitor grid as the input to another radiation hydrodynamics code, SNEC, and find that the output is consistent with that of STELLA, suggesting that our results are robust against the treatments on radiative transfer.

Applying the above findings to a sample of SNe II, we find that the distribution of M_{Henv} estimated from the observed light curves is considerably broader than the ones predicted by single star models evolving with standard stellar wind (Figure 9). This inconsistency suggests that a large fraction of SNe II experience substantial mass-loss before the onset of the core-collapse, pointing to missing ingredients in our estimation of the mass-loss rate, either in the standard wind mass-loss or binary interaction, or both, to account for the diversity in M_{Henv} , particularly at the low-mass end.

However, it is important to address several limitations in this work. Firstly, we have assumed that the microphysics, such as convection and overshooting, are fixed throughout the study. In practice, these factors may depend on M_{ZAMS} , the evolution phases, or vary on a case-by-case basis. For example, by adjusting the mixing length in the hydrogen-rich envelope and the overshooting parameters, [Goldberg et al. \(2019\)](#) generated progenitors with large M_{Henv} but small R , which are missing in our model grid (see also [Dessart et al. 2013](#)). Further, the mass-loss process is not self-consistently modeled. These factors potentially modify the structure of the hydrogen-rich envelope, and eventually affect the light curve at the plateau phase. Developing robust theory of convection would benefit from detailed 3D simulations of RSG (see [Goldberg et al. 2022a,b](#) for recent progress). In the future, the advance in observational techniques will provide better constrain on the RSG mass-loss rates and the binary fractions of massive stars. A comprehensive analysis that includes all these factors will improve the accuracy of the results in this work.

Although the hydrogen-rich envelope is very sensitive to the mass-loss history, it is important to note that the nucleosynthesis products within the helium core are hardly affected by the stripping of the outer envelope, but primarily determined by the helium core mass (e.g., [Takahashi et al. 2023](#)). The nebular observation, during which the ejecta become transparent and the intermediate-mass elements are exposed, is an useful tool to constrain the properties of the material in

the innermost region ([Wheeler et al. 2015](#); [Haynie & Piro 2023](#)). In particular, the strength of the oxygen emission [O I] is considered as a reliable measurement of M_{ZAMS} of the progenitor from theoretical ground ([Fransson & Chevalier 1989](#); [Maeda et al. 2007](#); [Jerkstrand et al. 2012, 2014, 2015](#); [Jerkstrand 2017](#); [Dessart & Hillier 2020](#); [Dessart et al. 2021a,b, 2023](#)), which is further applied to samples of observational data (see, e.g., [Kuncarayakti et al. 2015](#); [Fang & Maeda 2018](#); [Fang et al. 2019, 2022](#); [Prentice et al. 2019](#); [Terreran et al. 2019](#); [Hiramatsu et al. 2021a](#)). By directly comparing the results obtained from nebular spectroscopy and light curve modeling, it becomes possible to establish the relationship between M_{ZAMS} and the properties of the envelope, thus linking the progenitors with the mass-loss histories they experienced prior to their explosion as SNe II (Fang et al., in preparation).

- 1 The authors thank Takashi Nagao for reading the
- 2 manuscript and providing valuable comments. KM
- 3 acknowledges support from the Japan Society for
- 4 the Promotion of Science (JSPS) KAKENHI grant
- 5 (JP20H00174). TJM is supported by the Grants-in-
- 6 Aid for Scientific Research of the Japan Society for
- 7 the Promotion of Science (JP20H00174, JP21K13966,
- 8 JP21H04997). TM acknowledges support from the
- 9 Hakubi project at Kyoto University.

Software: [MESA](#) ([Paxton et al. 2011, 2013, 2015, 2018, 2019](#)); [SNEC](#) ([Morozova et al. 2015](#)); [SciPy](#) ([Virtanen et al. 2020](#)); [NumPy](#) ([Harris et al. 2020](#)); [Astropy](#) ([Astropy Collaboration et al. 2013, 2018](#)); [Matplotlib](#) ([Hunter 2007](#))

APPENDIX

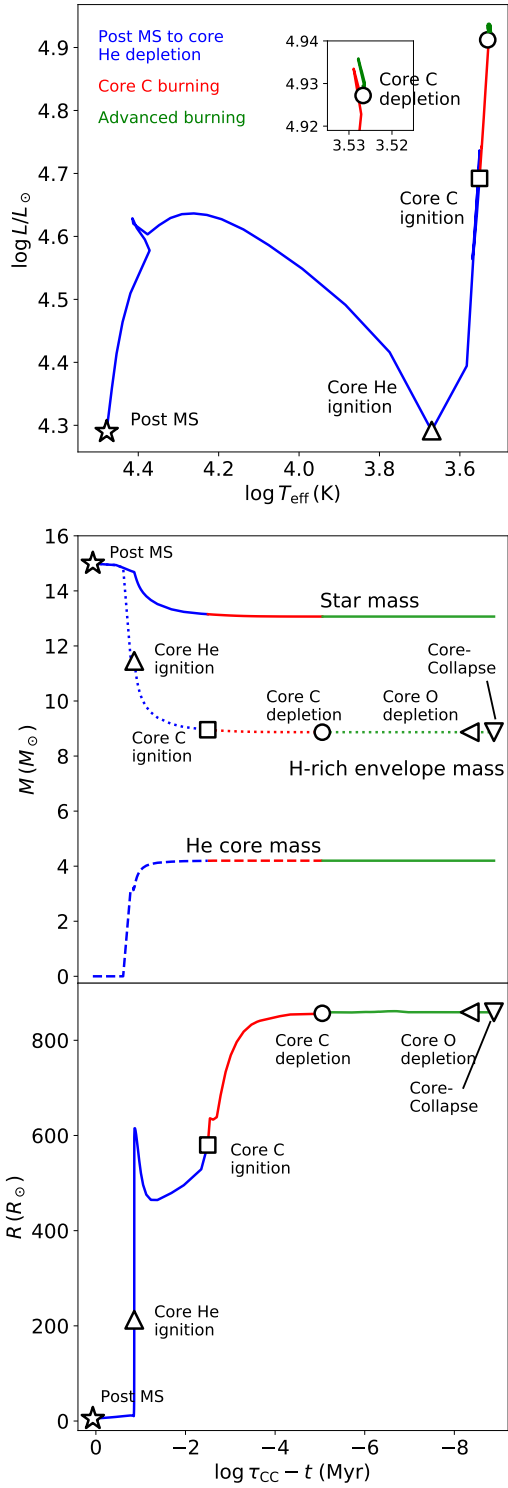


Figure 13. Upper panel: The evolution track of the progenitor model with $M_{ZAMS} = 15 M_{\odot}$ and $\eta = 1.0$ on the HR diagram, from post MS to core-collapse. Different evolution phases are labeled by different colors. Some special checkpoints are also marked; Middle panel: The evolution of star mass (solid), hydrogen-rich envelope mass (dotted) and He core mass (dashed), shown for the time relative to the moment of core-collapse (τ_{cc}); Lower panel: The evolution of stellar radius.

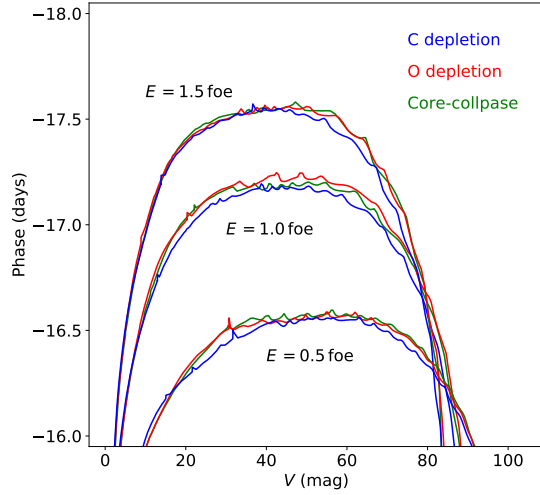


Figure 14. The V -band light curves calculated from the progenitor structures taken at different moments: core carbon depletion (blue; this work), core oxygen depletion (red) and core-collapse (green).

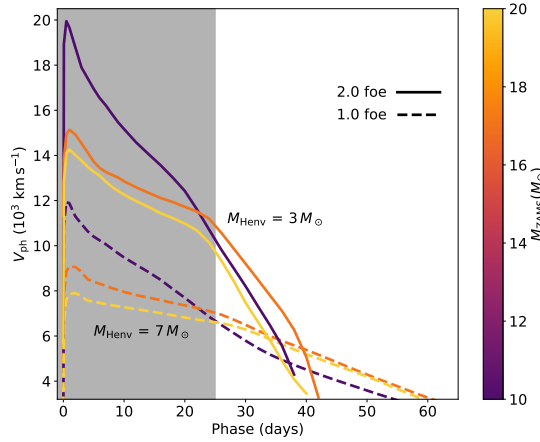


Figure 15. The photosphere evolution of some typical models. For models with the same M_{Henv} but varied M_{ZAMS} , the most pronounced differences in V_{ph} arise before ~ 25 days (the shaded region).

Table A1. SNe II sample in this work.

Name	t_{exp} (MJD)	$E(B - V)$ (mag)	μ (mag)	M_{Ni} (M_{\odot})	t_{p} (days)	$t_{\text{p},0}$ (days)	V_{p} (mag)	M_{Henv} (M_{\odot})	Ref.
1986L	46708	0.03	31.72 (0.20)	0.058 (0.046)	111.6 (6.0)	88.2 (12.0)	-17.18 (0.20)	9.63 (2.98)	a,b
1992af	48791	0.00	34.33 (0.12)	0.052 (0.040)	72.2 (6.0)	48.93 (11.84)	-17.08 (0.12)	3.06 (1.52)	a,b
1992ba	48888	0.02	31.07 (0.30)	0.019 (0.006)	125.05 (8.0)	99.81 (11.39)	-15.71 (0.30)	7.00 (1.50)	a,b,c
1995ad	49981	0.04	31.80 (0.15)	0.029 (0.014)	79.55 (3.0)	57.50 (10.76)	-16.41 (0.15)	3.23 (0.60)	d
1999em	51475	0.06	30.34 (0.07)	0.054 (0.011)	123.53 (1.0)	90.38 (8.40)	-16.62 (0.07)	8.17 (0.90)	a,b,c,e
1999gi	51518	0.19	30.34 (0.14)	0.032 (0.002)	121.98 (3.1)	83.87 (6.52)	-15.73 (0.14)	5.09 (0.70)	b,c,f
2001X	51963	0.07	31.59 (0.11)	0.055 (0.005)	114.51 (5.0)	79.32 (7.72)	-16.61 (0.11)	6.37 (1.07)	b,g,h
2002gw	52560	0.14	32.98 (0.22)	0.024 (0.006)	102.21 (3.0)	76.99 (7.93)	-15.98 (0.22)	4.76 (0.78)	a,b,i,j
2002hj	52563	0.10	34.91 (0.15)	0.030 (0.024)	101.55 (7.0)	79.18 (12.24)	-16.45 (0.15)	5.99 (2.01)	a,b,i
2002hx	52580	0.18	35.53 (0.08)	0.066 (0.010)	72.49 (3.7)	41.44 (7.52)	-16.96 (0.08)	2.14 (0.63)	a,b,i,j
2003B	52622	0.05	30.62 (0.25)	0.006 (0.02)	100.27 (4.2)	82.21 (7.86)	-14.78 (0.25)	3.44 (0.57)	a,b,i,j
2003T	52655	0.03	35.36 (0.15)	0.046 (0.011)	103.64 (10.0)	65.15 (13.76)	-16.21 (0.15)	3.79 (1.26)	b,k
2003Z	52665	0.03	31.70 (0.60)	0.005 (0.003)	120.40 (4.5)	101.89 (10.40)	-14.33 (0.60)	4.34 (0.96)	b,k
2003bn	52695	0.06	33.55 (0.15)	0.026 (0.020)	118.40 (3.0)	96.58 (9.90)	-16.26 (0.15)	8.09 (1.99)	a,b
2003bl	52700	0.02	34.07 (0.30)	0.009 (0.008)	104.74 (3.0)	83.63 (10.41)	-15.10 (0.30)	4.00 (1.16)	a,b,l
2003cx	52729	0.08	35.91 (0.15)	0.032 (0.025)	94.06 (5.0)	71.50 (11.40)	-16.52 (0.15)	5.06 (1.73)	a,b
2003fb	52779	0.37	34.05 (0.13)	0.034 (0.008)	95.70 (4.0)	51.58 (11.36)	-15.58 (0.13)	1.93 (0.46)	j,k
2003hd	52858	0.01	36.02 (0.15)	0.036 (0.004)	94.09 (5.0)	72.21 (7.57)	-16.72 (0.15)	5.56 (1.09)	a,b
2003hg	52866	0.06	33.65 (0.16)	0.014 (0.011)	123.85 (5.0)	102.05 (10.65)	-15.66 (0.16)	7.17 (1.68)	a,b,l
2003hk	52868	0.14	34.77 (0.12)	0.028 (0.007)	86.09 (3.0)	73.32 (6.39)	-17.22 (0.12)	6.91 (1.12)	j,k,m
2003hl	52869	0.06	32.16 (0.10)	0.011 (0.008)	135.60 (5.0)	114.05 (10.75)	-15.30 (0.10)	7.71 (1.62)	a,b,g
2003hn	52857	0.13	31.14 (0.26)	0.032 (0.005)	106.68 (4.0)	84.82 (7.19)	-16.58 (0.26)	7.14 (1.24)	a,b,c
2003iq	52920	0.06	32.16 (0.10)	0.049 (0.009)	95.46 (2.0)	53.10 (8.50)	-16.12 (0.10)	2.49 (0.48)	a,b,g
2004A	53012	0.18	30.87 (0.26)	0.026 (0.007)	118.19 (2.0)	89.85 (8.63)	-15.90 (0.26)	6.17 (0.88)	j,n,o
2004dj	53181	0.09	27.46 (0.11)	0.013 (0.004)	110.09 (15.6)	92.30 (16.95)	-15.80 (0.11)	6.25 (2.13)	j,p,q,r,s
2004ej	53232	0.14	33.1 (0.21)	0.017 (0.007)	105.53 (4.2)	92.88 (7.28)	-16.63 (0.21)	8.63 (1.38)	a,j
2004er	53272	0.13	33.83 (0.15)	0.033 (0.026)	150.59 (2.0)	127.96 (10.51)	-16.55 (0.15)	15.28 (2.89)	a,b
2004et	53270	0.41	28.36 (0.09)	0.068 (0.009)	123.50 (4.0)	85.42 (7.69)	-16.70 (0.09)	7.58 (1.10)	b,t,u
2004fx	53304	0.09	32.71 (0.15)	0.017 (0.007)	102.14 (4.0)	73.19 (12.37)	-15.43 (0.15)	3.52 (0.64)	a,b
2005J	53383	0.22	33.96 (0.14)	0.059 (0.045)	114.37 (7.0)	90.86 (12.32)	-17.21 (0.14)	10.29 (3.04)	a,b,j
2005ay	53450	0.04	30.68 (0.21)	0.017 (0.004)	114.35 (1.8)	83.41 (8.94)	-15.35 (0.21)	4.37 (0.62)	j,v
2005cs	53548	0.05	29.26 (0.33)	0.002 (0.001)	125.61 (0.5)	115.69 (5.29)	-14.65 (0.33)	6.22 (0.94)	a,b,j,v,w,x
2005dk	53600	0.00	34.01 (0.14)	0.044 (0.034)	99.76 (6.0)	76.44 (11.89)	-16.88 (0.14)	6.58 (2.16)	a,b
2005dx	53616	0.09	35.09 (0.09)	0.010 (0.004)	100.76 (4.6)	84.17 (9.17)	-15.54 (0.08)	4.77 (0.73)	a,b,j
2005dz	53620	0.07	34.44 (0.15)	0.024 (0.018)	112.51 (4.0)	90.86 (9.93)	-16.17 (0.15)	6.98 (1.82)	a,b
2006Y	53767	0.11	35.70 (0.06)	0.044 (0.032)	67.19 (4.0)	43.86 (10.91)	-16.88 (0.06)	2.31 (1.16)	a,b,y
2006ai	53782	0.11	34.01 (0.14)	0.054 (0.041)	71.32 (5.0)	47.81 (11.31)	-17.11 (0.14)	2.96 (1.44)	a,b,y
2006ee	53962	0.00	33.87 (0.15)	0.020 (0.015)	106.69 (4.0)	85.23 (9.72)	-15.98 (0.15)	5.77 (1.58)	a

Table A1 continued

Table A1 (continued)

Name	t_{exp} (MJD)	$E(B - V)$ (mag)	μ (mag)	M_{Ni} (M_{\odot})	t_{p} (days)	$t_{\text{p},0}$ (days)	V_{p} (mag)	M_{Henv} (M_{\odot})	Ref.
2006ov	53974	0.02	30.50 (0.95)	0.002 (0.002)	120.84 (6.0)	111.52 (8.42)	-14.80 (0.95)	6.14 (2.54)	k
2007ab	54124	0.23	34.97 (0.15)	0.048 (0.038)	73.16 (10.0)	49.56 (14.49)	-16.96 (0.15)	3.00 (1.76)	a,b
2007it	54349	0.42	30.35 (0.36)	0.108 (0.033)	112.62 (10.0)	87.08 (13.17)	-17.74 (0.36)	11.56 (3.54)	a,b,j,z
2007od	54388	0.04	32.05 (0.15)	0.020 (0.010)	135.83 (4.1)	125.56 (6.99)	-17.28 (0.15)	19.41 (2.18)	aa
2007sq	54422	0.00	34.12 (0.13)	0.004 (0.003)	105.81 (4.0)	89.48 (8.11)	-14.41 (0.13)	3.50 (0.80)	a
2008K	54478	0.09	35.29 (0.10)	0.027 (0.012)	93.45 (4.0)	74.72 (9.21)	-16.54 (0.10)	5.55 (0.92)	a,b,j
2008M	54475	0.09	32.62 (0.20)	0.027 (0.011)	81.43 (3.3)	61.14 (9.26)	-16.43 (0.20)	3.65 (0.73)	a,b,j
2008W	54486	0.00	34.59 (0.11)	0.019 (0.015)	97.57 (6.0)	76.83 (10.55)	-15.99 (0.11)	4.76 (1.50)	a
2008aw	54518	0.14	33.21 (0.15)	0.087 (0.023)	77.93 (4.0)	51.07 (9.07)	-17.45 (0.17)	3.81 (0.97)	a,b,j
2008bk	54543	0.02	27.68 (0.13)	0.007 (0.001)	131.65 (2.0)	110.84 (6.27)	-14.73 (0.13)	5.91 (0.59)	ab,ac
2008bx	54576	0.02	32.99 (0.80)	0.033 (0.051)	87.88 (4.0)	65.71 (12.83)	-16.60 (0.80)	4.47 (4.19)	ad
2008ea	54646	0.12	33.77 (0.16)	0.010 (0.008)	93.94 (8.0)	73.42 (12.23)	-15.30 (0.16)	3.38 (1.19)	ad
2008ga	54712	0.00	33.99 (0.14)	0.005 (0.004)	87.60 (4.0)	70.54 (8.33)	-14.51 (0.14)	2.34 (0.69)	ad
2008if	54808	0.10	33.54 (0.15)	0.057 (0.045)	83.96 (5.0)	61.03 (11.27)	-17.20 (0.15)	4.84 (1.96)	a,b
2008in	54808	0.05	30.45 (0.10)	0.004 (0.001)	107.83 (1.0)	96.75 (5.43)	-15.07 (0.10)	5.21 (0.57)	a,b,ae,af
2009N	54848	0.05	31.67 (0.11)	0.016 (0.002)	108.67 (1.2)	80.85 (6.20)	-15.44 (0.11)	4.26 (0.55)	a,b,ag
2009at	54899	0.55	31.82 (0.22)	0.018 (0.005)	75.90 (2.0)	62.53 (6.00)	-16.59 (0.22)	4.05 (0.75)	j,ad
2009bw	54916	0.28	31.44 (0.15)	0.023 (0.002)	136.13 (3.0)	119.53 (6.14)	-16.54 (0.15)	13.44 (1.42)	a,b,ah
2009dd	54916	0.45	30.74 (0.15)	0.060 (0.014)	126.66 (4.2)	106.42 (10.44)	-16.54 (0.15)	7.58 (1.15)	d,j,ai
2009ib	55041	0.16	31.48 (0.31)	0.045 (0.008)	140.65 (2.0)	91.47 (8.58)	-15.75 (0.31)	6.02 (0.89)	j,aj
2009kr	55140	0.07	32.09 (0.15)	0.008 (0.001)	82.97 (2.0)	70.10 (5.62)	-15.84 (0.15)	3.78 (0.59)	b,ak
2009md	55162	0.12	31.66 (0.15)	0.004 (0.003)	117.86 (8.0)	103.74 (11.46)	-14.72 (0.15)	5.20 (0.94)	b,al
2011ef	55760	0.06	33.60 (0.18)	0.050 (0.032)	117.41 (1.0)	94.85 (10.46)	-16.90 (0.18)	9.57 (2.41)	ad
2012A	55932	0.04	29.96 (0.15)	0.009 (0.001)	106.94 (2.0)	92.07 (5.81)	-15.61 (0.15)	5.79 (0.70)	b,am
2012aw	56002	0.08	29.96 (0.09)	0.050 (0.006)	135.74 (4.0)	104.33 (7.36)	-16.61 (0.09)	10.63 (1.26)	b,k,af,an
2012ck	56064	0.08	36.30 (0.05)	0.071 (0.055)	76.28 (2.0)	53.48 (10.18)	-17.44 (0.05)	4.14 (1.71)	ad
2012ec	56143	0.14	31.32 (0.15)	0.039 (0.005)	106.94 (5.0)	83.84 (7.74)	-16.75 (0.15)	7.45 (1.28)	b,ao
2013K	56302	0.25	32.66 (0.50)	0.012 (0.010)	131.40 (5.0)	113.43 (12.74)	-15.69 (0.50)	8.83 (1.99)	ap
2013ab	56340	0.04	31.90 (0.08)	0.064 (0.003)	102.12 (1.0)	65.24 (5.50)	-16.68 (0.08)	4.53 (0.71)	aq
2013am	56372	0.65	30.54 (0.40)	0.015 (0.006)	108.92 (2.0)	92.06 (7.37)	-16.02 (0.40)	6.76 (1.28)	ap
2013bu	56400	0.08	30.79 (0.08)	0.002 (0.001)	102.47 (4.5)	91.89 (7.11)	-14.45 (0.08)	3.74 (0.52)	b,ar
2013by	56404	0.23	30.81 (0.15)	0.032 (0.004)	84.79 (2.0)	71.95 (5.71)	-17.39 (0.15)	7.09 (1.11)	b,as
2013ej	56496	0.06	29.79 (0.20)	0.021 (0.002)	100.82 (1.0)	86.55 (5.42)	-16.62 (0.20)	7.52 (1.01)	b,at,au
2013fs	56571	0.04	33.45 (0.15)	0.054 (0.001)	80.20 (0.5)	52.75 (5.28)	-16.91 (0.15)	3.30 (0.64)	b,av
2013hj	56637	0.10	32.25 (0.15)	0.080 (0.008)	102.53 (1.5)	74.70 (5.97)	-17.32 (0.15)	7.40 (1.09)	aw
LSQ13dpa	56643	0.04	35.08 (0.15)	0.071 (0.013)	129.02 (2.0)	91.88 (7.74)	-16.80 (0.15)	9.00 (1.12)	a,b
2014G	56668	0.21	31.90 (0.15)	0.034 (0.001)	87.12 (1.0)	72.29 (5.35)	-17.22 (0.15)	6.71 (0.99)	aw,ax
2014cx	56902	0.10	31.27 (0.47)	0.056 (0.008)	109.52 (1.0)	71.37 (7.13)	-16.47 (0.47)	4.95 (1.05)	ay
2014cy	56900	0.36	31.85 (0.34)	0.027 (0.006)	124.90 (1.0)	104.45 (6.78)	-16.43 (0.34)	9.98 (1.53)	az
2014dw	56958	0.22	32.46 (0.15)	0.009 (0.001)	91.90 (10.0)	80.85 (11.30)	-16.25 (0.15)	5.78 (1.58)	b

Table A1 continued

Table A1 (continued)

Name	t_{exp} (MJD)	$E(B - V)$ (mag)	μ (mag)	M_{Ni} (M_{\odot})	t_{p} (days)	$t_{\text{p},0}$ (days)	V_{p} (mag)	M_{Henv} (M_{\odot})	Ref.
ASASSN-14dq	56841	0.07	33.26 (0.15)	0.046 (0.008)	100.99 (5.5)	78.01 (8.36)	-16.94 (0.15)	6.99 (1.34)	b
ASASSN-14gm	56901	0.10	31.74 (0.15)	0.077 (0.010)	110.57 (1.5)	78.22 (6.55)	-17.07 (0.15)	7.37 (1.02)	b
ASASSN-14ha	56910	0.01	29.53 (0.50)	0.010 (0.003)	136.50 (1.5)	100.72 (11.49)	-14.36 (0.50)	4.31 (0.69)	b
2015V	57112	0.03	31.63 (0.22)	0.023 (0.006)	116.31 (4.3)	83.40 (9.50)	-15.59 (0.22)	4.77 (0.81)	j,ad
2015an	57268	0.09	32.42 (0.13)	0.021 (0.010)	130.21 (1.6)	114.48 (7.41)	-16.48 (0.13)	12.09 (1.20)	ba
2015cz	57298	0.48	34.02 (0.20)	0.070 (0.010)	113.26 (4.3)	89.70 (7.37)	-17.38 (0.20)	10.70 (1.05)	az
2016B	57382	0.08	32.14 (0.40)	0.082 (0.019)	133.71 (1.2)	92.90 (9.33)	-16.82 (0.40)	9.26 (1.63)	bb
2016X	57406	0.04	30.91 (0.43)	0.034 (0.006)	94.97 (0.6)	67.96 (6.92)	-16.34 (0.43)	4.30 (0.85)	bc
2016gfy	57641	0.21	32.36 (0.18)	0.033 (0.003)	112.72 (0.9)	93.14 (5.55)	-16.76 (0.18)	9.11 (1.12)	bd
2017it	57747	0.03	36.48 (0.12)	0.100 (0.010)	109.20 (1.0)	75.81 (6.02)	-17.32 (0.12)	7.61 (1.04)	be
2017ahn	57792	0.26	32.59 (0.43)	0.041 (0.006)	56.17 (0.5)	40.66 (5.51)	-17.34 (0.43)	2.39 (0.72)	bf,bg
2017eaw	57886	0.41	29.18 (0.20)	0.115 (0.027)	117.08 (1.0)	78.01 (9.39)	-17.26 (0.20)	7.87 (1.13)	bh,bi,bj
2017gmr	57999	0.30	31.46 (0.15)	0.142 (0.031)	96.54 (1.0)	68.65 (7.48)	-17.91 (0.15)	7.90 (1.29)	bk,bl,bm
2018gj	58128	0.08	31.46 (0.15)	0.026 (0.007)	77.84 (1.4)	58.56 (7.02)	-16.46 (0.15)	3.41 (0.59)	bn
2018zd	58178	0.17	29.91 (0.22)	0.009 (0.001)	116.59 (1.0)	103.86 (5.35)	-15.92 (0.22)	8.18 (1.04)	bo,bp,bq,br
2018cuf	58292	0.14	33.10 (0.30)	0.040 (0.010)	111.24 (1.0)	85.46 (8.02)	-16.62 (0.30)	7.35 (1.13)	bs
2018hfm	58395	0.31	32.79 (0.64)	0.015 (0.005)	57.21 (5.3)	48.23 (7.52)	-17.39 (0.64)	3.35 (1.29)	bt
2018hwm	58425	0.02	33.58 (0.19)	0.003 (0.002)	144.41 (1.0)	133.83 (15.85)	-14.94 (0.19)	9.10 (0.91)	bu
2020jfo	58974	0.02	30.81 (0.20)	0.018 (0.007)	66.15 (2.0)	49.00 (7.55)	-16.18 (0.20)	2.20 (0.50)	bv,bw,bx,by
2021gmj	59293	0.06	31.42 (0.20)	0.020 (0.004)	106.24 (1.0)	77.28 (7.25)	-15.60 (0.20)	4.16 (0.61)	bz
2021yja	59465	0.10	31.85 (0.45)	0.141 (0.050)	124.26 (1.5)	77.66 (15.33)	-17.26 (0.45)	7.79 (2.01)	ca,cb,cc

Note—The columns are (from left to right): SN name, date of explosion, extinction, distance module, nickel mass, plateau duration, plateau duration corrected for nickel heating, plateau magnitude, hydrogen-rich envelope mass, references. References: a:Anderson et al. (2014); b:Valenti et al. (2016); c:Jones et al. (2009); d:Inserra et al. (2013); e:Leonard et al. (2003); f:Leonard et al. (2002); g:Poznanski et al. (2009); h:Faran et al. (2014a); i:Galbany et al. (2016); j:Rodríguez et al. (2021); k:Spiro et al. (2014); l:Olivares E. et al. (2010); m:Faran et al. (2014b); n:Gurugubelli et al. (2008); o:Hendry et al. (2006); p:Vinkó et al. (2006); q:Zhang et al. (2006); r:Tsvetkov et al. (2008); s:Vinkó et al. (2009); t:Utrobin & Chugai (2009); u:Maguire et al. (2010); v:Tsvetkov et al. (2006); w:Takáts & Vinkó (2006); x:Pastorello et al. (2009); y:Hiramatsu et al. (2021a); z:Andrews et al. (2011); aa:Inserra et al. (2011); ab:Pignata (2013); ac:Van Dyk et al. (2012a); ad:de Jaeger et al. (2019); ae:Roy et al. (2011); af:Bose & Kumar (2014); ag:Takáts et al. (2014); ah:Inserra et al. (2012); ai:Hicken et al. (2017); aj:Takáts et al. (2015); ak:Elias-Rosa et al. (2010); al:Fraser et al. (2011); am:Tomasella et al. (2013); an:Dall’Ora et al. (2014); ao:Barbarino et al. (2015); ap:Tomasella et al. (2018); aq:Bose et al. (2015); ar:Kanbur et al. (2003); as:Valenti et al. (2015); at:Fraser et al. (2014); au:Valenti et al. (2014); av:Yaron et al. (2017); aw:Bose et al. (2016); ax:Terreran et al. (2016); ay:Huang et al. (2016); az:Dastidar et al. (2021); ba:Dastidar et al. (2019a); bb:Dastidar et al. (2019b); bc:Huang et al. (2018); bd:Singh et al. (2019); be:Afsariardchi et al. (2019); bf:Tartaglia et al. (2021); bg:Nagao et al. (2021); bh:Tsvetkov et al. (2018); bi:Buta & Keel (2019); bj:Szalai et al. (2019); bk:Andrews et al. (2019); bl:Nagao et al. (2019); bm:Utrobin et al. (2021); bn:Teja et al. (2023); bo:Zhang et al. (2020); bp:Hiramatsu et al. (2021b); bq:Callis et al. (2021); br:Tsvetkov et al. (2022); bs:Dong et al. (2021); bt:Zhang et al. (2022); bu:Reguitti et al. (2021); bv:Sollerman et al. (2021); bw:Teja et al. (2022); bx:Ailawadhi et al. (2023); by:Kilpatrick et al. (2023b); bz:Murai et al. (2024); ca:Vasylyev et al. (2022); cb:Kozyreva et al. (2022); cc:Hosseinzadeh et al. (2022)

REFERENCES

- Afsariardchi, N., Moon, D.-S., Drout, M. R., et al. 2019, *ApJ*, 881, 22. doi:10.3847/1538-4357/ab2be6
- Ailawadhi, B., Dastidar, R., Misra, K., et al. 2023, *MNRAS*, 519, 248. doi:10.1093/mnras/stac3234
- Anderson, J. P., González-Gaitán, S., Hamuy, M., et al. 2014, *ApJ*, 786, 67. doi:10.1088/0004-637X/786/1/67
- Anderson, J. P. 2019, *A&A*, 628, A7. doi:10.1051/0004-6361/201935027
- Andrews, J. E., Sugerman, B. E. K., Clayton, G. C., et al. 2011, *ApJ*, 731, 47. doi:10.1088/0004-637X/731/1/47
- Andrews, J. E., Sand, D. J., Valenti, S., et al. 2019, *ApJ*, 885, 43. doi:10.3847/1538-4357/ab43e3
- Arnett, W. D. 1982, *ApJ*, 253, 785. doi:10.1086/159681
- Arnett, W. D. & Fu, A. 1989, *ApJ*, 340, 396. doi:10.1086/167402
- Astropy Collaboration, Robitaille, T. P., Tollerud, E. J., et al. 2013, *A&A*, 558, A33. doi:10.1051/0004-6361/201322068
- Astropy Collaboration, Price-Whelan, A. M., Sipőcz, B. M., et al. 2018, *AJ*, 156, 123. doi:10.3847/1538-3881/aabc4f
- Barbarino, C., Dall’Ora, M., Botticella, M. T., et al. 2015, *MNRAS*, 448, 2312. doi:10.1093/mnras/stv106
- Barker, B. L., Harris, C. E., Warren, M. L., et al. 2022, *ApJ*, 934, 67. doi:10.3847/1538-4357/ac77f3
- Barker, B. L., O’Connor, E. P., & Couch, S. M. 2023, *ApJL*, 944, L2. doi:10.3847/2041-8213/acb052
- Beasor, E. R., Davies, B., Smith, N., et al. 2020, *MNRAS*, 492, 5994. doi:10.1093/mnras/staa255
- Bersten, M. C., Benvenuto, O., & Hamuy, M. 2011, *ApJ*, 729, 61. doi:10.1088/0004-637X/729/1/61
- Blinnikov, S. I., Eastman, R., Bartunov, O. S., et al. 1998, *ApJ*, 496, 454. doi:10.1086/305375
- Blinnikov, S., Lundqvist, P., Bartunov, O., et al. 2000, *ApJ*, 532, 1132. doi:10.1086/308588
- Blinnikov, S. I., Röpke, F. K., Sorokina, E. I., et al. 2006, *A&A*, 453, 229. doi:10.1051/0004-6361:20054594
- Bose, S. & Kumar, B. 2014, *ApJ*, 782, 98. doi:10.1088/0004-637X/782/2/98
- Bose, S., Valenti, S., Misra, K., et al. 2015, *MNRAS*, 450, 2373. doi:10.1093/mnras/stv759
- Burrows, A. & Vartanyan, D. 2021, *Nature*, 589, 29. doi:10.1038/s41586-020-03059-w
- Bose, S., Kumar, B., Misra, K., et al. 2016, *MNRAS*, 455, 2712. doi:10.1093/mnras/stv2351
- Buta, R. J. & Keel, W. C. 2019, *MNRAS*, 487, 832. doi:10.1093/mnras/stz1291
- Callis, E., Fraser, M., Pastorello, A., et al. 2021, arXiv:2109.12943. doi:10.48550/arXiv.2109.12943
- Chen, P., Gal-Yam, A., Sollerman, J., et al. 2023, arXiv:2310.07784. doi:10.48550/arXiv.2310.07784
- Crockett, R. M., Smartt, S. J., Pastorello, A., et al. 2011, *MNRAS*, 410, 2767. doi:10.1111/j.1365-2966.2010.17652.x
- Dall’Ora, M., Botticella, M. T., Pumo, M. L., et al. 2014, *ApJ*, 787, 139. doi:10.1088/0004-637X/787/2/139
- Davies, B. & Beasor, E. R. 2018, *MNRAS*, 474, 2116. doi:10.1093/mnras/stx2734
- Davies, B. & Beasor, E. R. 2020, *MNRAS*, 493, 468. doi:10.1093/mnras/staa174
- Dastidar, R., Misra, K., Valenti, S., et al. 2019, *MNRAS*, 490, 1605. doi:10.1093/mnras/stz2703
- Dastidar, R., Misra, K., Singh, M., et al. 2019, *MNRAS*, 486, 2850. doi:10.1093/mnras/stz949
- Dastidar, R., Misra, K., Singh, M., et al. 2021, *MNRAS*, 504, 1009. doi:10.1093/mnras/stab831
- de Jager, C., Nieuwenhuijzen, H., & van der Hucht, K. A. 1988, *A&AS*, 72, 259
- de Jaeger, T., Zheng, W., Stahl, B. E., et al. 2019, *MNRAS*, 490, 2799. doi:10.1093/mnras/stz2714
- Dessart, L., Hillier, D. J., Waldman, R., et al. 2013, *MNRAS*, 433, 1745. doi:10.1093/mnras/stt861
- Dessart, L. & Hillier, D. J. 2019, *A&A*, 625, A9. doi:10.1051/0004-6361/201834732
- Dessart, L. & Hillier, D. J. 2020, *A&A*, 642, A33. doi:10.1051/0004-6361/202038148
- Dessart, L., Hillier, D. J., Sukhbold, T., et al. 2021, *A&A*, 652, A64. doi:10.1051/0004-6361/202140839
- Dessart, L., Hillier, D. J., Sukhbold, T., et al. 2021, *A&A*, 656, A61. doi:10.1051/0004-6361/202141927
- Dessart, L., Hillier, D. J., Woosley, S. E., et al. 2023, *A&A*, 677, A7. doi:10.1051/0004-6361/202346626
- Dessart, L., Gutierrez, C. P., Ercolino, A., et al. 2024, arXiv:2402.12977. doi:10.48550/arXiv.2402.12977
- Dong, Y., Valenti, S., Bostroem, K. A., et al. 2021, *ApJ*, 906, 56. doi:10.3847/1538-4357/abc417
- Drout, M. R., Götzberg, Y., Ludwig, B. A., et al. 2023, arXiv:2307.00061. doi:10.48550/arXiv.2307.00061
- Eldridge, J. J. & Vink, J. S. 2006, *A&A*, 452, 295. doi:10.1051/0004-6361:20065001
- Eldridge, J. J., Izzard, R. G., & Tout, C. A. 2008, *MNRAS*, 384, 1109. doi:10.1111/j.1365-2966.2007.12738.x
- Eldridge, J. J., Fraser, M., Smartt, S. J., et al. 2013, *MNRAS*, 436, 774. doi:10.1093/mnras/stt1612
- Eldridge, J. J., Xiao, L., Stanway, E. R., et al. 2018, *PASA*, 35, e049. doi:10.1017/pasa.2018.47
- Elias-Rosa, N., Van Dyk, S. D., Li, W., et al. 2010, *ApJL*, 714, L254. doi:10.1088/2041-8205/714/2/L254

- Elias-Rosa, N., Van Dyk, S. D., Li, W., et al. 2011, *ApJ*, 742, 6. doi:10.1088/0004-637X/742/1/6
- Ercolino, A., Jin, H., Langer, N., et al. 2023, arXiv:2308.01819. doi:10.48550/arXiv.2308.01819
- Ertl, T., Janka, H.-T., Woosley, S. E., et al. 2016, *ApJ*, 818, 124. doi:10.3847/0004-637X/818/2/124
- Fang, Q. & Maeda, K. 2018, *ApJ*, 864, 47. doi:10.3847/1538-4357/aad096
- Fang, Q., Maeda, K., Kuncarayakti, H., et al. 2019, *Nature Astronomy*, 3, 434. doi:10.1038/s41550-019-0710-6
- Fang, Q., Maeda, K., Kuncarayakti, H., et al. 2022, *ApJ*, 928, 151. doi:10.3847/1538-4357/ac4f60
- Faran, T., Poznanski, D., Filippenko, A. V., et al. 2014, *MNRAS*, 442, 844. doi:10.1093/mnras/stu955
- Faran, T., Poznanski, D., Filippenko, A. V., et al. 2014, *MNRAS*, 445, 554. doi:10.1093/mnras/stu1760
- Farmer, R., Fields, C. E., Petermann, I., et al. 2016, *ApJS*, 227, 22. doi:10.3847/1538-4365/227/2/22
- Filippenko, A. V. 1997, *ARA&A*, 35, 309. doi:10.1146/annurev.astro.35.1.309
- Fragos, T., Andrews, J. J., Bavera, S. S., et al. 2023, *ApJS*, 264, 45. doi:10.3847/1538-4365/ac90c1
- Fransson, C. & Chevalier, R. A. 1989, *ApJ*, 343, 323. doi:10.1086/167707
- Fraser, M., Takáts, K., Pastorello, A., et al. 2010, *ApJL*, 714, L280. doi:10.1088/2041-8205/714/2/L280
- Fraser, M., Ergon, M., Eldridge, J. J., et al. 2011, *MNRAS*, 417, 1417. doi:10.1111/j.1365-2966.2011.19370.x
- Fraser, M., Maund, J. R., Smartt, S. J., et al. 2012, *ApJL*, 759, L13. doi:10.1088/2041-8205/759/1/L13
- Fraser, M., Maund, J. R., Smartt, S. J., et al. 2014, *MNRAS*, 439, L56. doi:10.1093/mnras/slt179
- Gal-Yam, A. 2017, *Handbook of Supernovae*, 195. doi:10.1007/978-3-319-21846-5_35
- Galbany, L., Hamuy, M., Phillips, M. M., et al. 2016, *AJ*, 151, 33. doi:10.3847/0004-6256/151/2/33
- Gilkis, A. & Arcavi, I. 2022, *MNRAS*, 511, 691. doi:10.1093/mnras/stac088
- Glebbeek, E., Gaburov, E., de Mink, S. E., et al. 2009, *A&A*, 497, 255. doi:10.1051/0004-6361/200810425
- Goldberg, J. A., Bildsten, L., & Paxton, B. 2019, *ApJ*, 879, 3. doi:10.3847/1538-4357/ab22b6
- Goldberg, J. A. & Bildsten, L. 2020, *ApJL*, 895, L45. doi:10.3847/2041-8213/ab9300
- Goldberg, J. A., Jiang, Y.-F., & Bildsten, L. 2022, *ApJ*, 929, 156. doi:10.3847/1538-4357/ac5ab3
- Goldberg, J. A., Jiang, Y.-F., & Bildsten, L. 2022, *ApJ*, 933, 164. doi:10.3847/1538-4357/ac75e3
- Groh, J. H., Georgy, C., & Ekström, S. 2013, *A&A*, 558, L1. doi:10.1051/0004-6361/201322369
- Gutiérrez, C. P., Anderson, J. P., Hamuy, M., et al. 2017, *ApJ*, 850, 89. doi:10.3847/1538-4357/aa8f52
- Gutiérrez, C. P., Anderson, J. P., Hamuy, M., et al. 2017, *ApJ*, 850, 90. doi:10.3847/1538-4357/aa8f42
- Gurugubelli, U. K., Sahu, D. K., Anupama, G. C., et al. 2008, *Bulletin of the Astronomical Society of India*, 36, 79
- Hamuy, M. 2003, *ApJ*, 582, 905. doi:10.1086/344689
- Harris, C. R., Millman, K. J., van der Walt, S. J., et al. 2020, *Nature*, 585, 357. doi:10.1038/s41586-020-2649-2
- Haynie, A. & Piro, A. L. 2023, *ApJ*, 956, 98. doi:10.3847/1538-4357/acf844
- Heger, A., Fryer, C. L., Woosley, S. E., et al. 2003, *ApJ*, 591, 288. doi:10.1086/375341
- Hendry, M. A., Smartt, S. J., Crockett, R. M., et al. 2006, *MNRAS*, 369, 1303. doi:10.1111/j.1365-2966.2006.10374.x
- Hicken, M., Friedman, A. S., Blondin, S., et al. 2017, *ApJS*, 233, 6. doi:10.3847/1538-4365/aa8ef4
- Hirai, R. 2023, *MNRAS*, 523, 6011. doi:10.1093/mnras/stad1856
- Hiramatsu, D., Howell, D. A., Moriya, T. J., et al. 2021, *ApJ*, 913, 55. doi:10.3847/1538-4357/abf6d6
- Hiramatsu, D., Howell, D. A., Van Dyk, S. D., et al. 2021, *Nature Astronomy*, 5, 903. doi:10.1038/s41550-021-01384-2
- Hosseinzadeh, G., Kilpatrick, C. D., Dong, Y., et al. 2022, *ApJ*, 935, 31. doi:10.3847/1538-4357/ac75f0
- Huang, F., Wang, X., Zampieri, L., et al. 2016, *ApJ*, 832, 139. doi:10.3847/0004-637X/832/2/139
- Huang, F., Wang, X.-F., Hosseinzadeh, G., et al. 2018, *MNRAS*, 475, 3959. doi:10.1093/mnras/sty066
- Hunter, J. D. 2007, *Computing in Science and Engineering*, 9, 90. doi:10.1109/MCSE.2007.55
- Inserra, C., Turatto, M., Pastorello, A., et al. 2011, *MNRAS*, 417, 261. doi:10.1111/j.1365-2966.2011.19128.x
- Inserra, C., Turatto, M., Pastorello, A., et al. 2012, *MNRAS*, 422, 1122. doi:10.1111/j.1365-2966.2012.20685.x
- Inserra, C., Pastorello, A., Turatto, M., et al. 2013, *A&A*, 555, A142. doi:10.1051/0004-6361/201220496
- Jencson, J. E., Pearson, J., Beasor, E. R., et al. 2023, arXiv:2306.08678. doi:10.48550/arXiv.2306.08678
- Jerkstrand, A., Fransson, C., Maguire, K., et al. 2012, *A&A*, 546, A28. doi:10.1051/0004-6361/201219528
- Jerkstrand, A., Smartt, S. J., Fraser, M., et al. 2014, *MNRAS*, 439, 3694. doi:10.1093/mnras/stu221
- Jerkstrand, A., Ergon, M., Smartt, S. J., et al. 2015, *A&A*, 573, A12. doi:10.1051/0004-6361/201423983
- Jerkstrand, A. 2017, *Handbook of Supernovae*, 795. doi:10.1007/978-3-319-21846-5_29
- Jones, M. I., Hamuy, M., Lira, P., et al. 2009, *ApJ*, 696, 1176. doi:10.1088/0004-637X/696/2/1176

- Kanbur, S. M., Ngeow, C., Nikolaev, S., et al. 2003, *A&A*, 411, 361. doi:10.1051/0004-6361:20031373
- Kasen, D. & Woosley, S. E. 2009, *ApJ*, 703, 2205. doi:10.1088/0004-637X/703/2/2205
- Khatami, D. & Kasen, D. 2023, arXiv:2304.03360. doi:10.48550/arXiv.2304.03360
- Kilpatrick, C. D., Foley, R. J., Jacobson-Galán, W. V., et al. 2023, arXiv:2306.04722. doi:10.48550/arXiv.2306.04722
- Kilpatrick, C. D., Izzo, L., Bentley, R. O., et al. 2023, *MNRAS*, 524, 2161. doi:10.1093/mnras/stad1954
- Kippenhahn, R., Ruschenplatt, G., & Thomas, H.-C. 1980, *A&A*, 91, 175
- Kochanek, C. S., Khan, R., & Dai, X. 2012, *ApJ*, 759, 20. doi:10.1088/0004-637X/759/1/20
- Kochanek, C. S., Fraser, M., Adams, S. M., et al. 2017, *MNRAS*, 467, 3347. doi:10.1093/mnras/stx291
- Kozyreva, A., Nakar, E., & Waldman, R. 2019, *MNRAS*, 483, 1211. doi:10.1093/mnras/sty3185
- Kozyreva, A., Klencki, J., Filippenko, A. V., et al. 2022, *ApJL*, 934, L31. doi:10.3847/2041-8213/ac835a
- Kudritzki, R.-P. & Puls, J. 2000, *ARA&A*, 38, 613. doi:10.1146/annurev.astro.38.1.613
- Kuncarayakti, H., Maeda, K., Bersten, M. C., et al. 2015, *A&A*, 579, A95. doi:10.1051/0004-6361/201425604
- Lamers, H. J. G. L. M. 1981, *ApJ*, 245, 593. doi:10.1086/158835
- Leonard, D. C., Filippenko, A. V., Li, W., et al. 2002, *AJ*, 124, 2490. doi:10.1086/343771
- Leonard, D. C., Kanbur, S. M., Ngeow, C. C., et al. 2003, *ApJ*, 594, 247. doi:10.1086/376831
- Li, W., Van Dyk, S. D., Filippenko, A. V., et al. 2006, *ApJ*, 641, 1060. doi:10.1086/499916
- Lisakov, S. M., Dessart, L., Hillier, D. J., et al. 2017, *MNRAS*, 466, 34. doi:10.1093/mnras/stw3035
- Maeda, K., Kawabata, K., Tanaka, M., et al. 2007, *ApJ*, 658, L5. doi:10.1086/513564
- Maeder, A. & Meynet, G. 2001, *A&A*, 373, 555. doi:10.1051/0004-6361:20010596
- Maguire, K., Di Carlo, E., Smartt, S. J., et al. 2010, *MNRAS*, 404, 981. doi:10.1111/j.1365-2966.2010.16332.x
- Martinez, L. & Bersten, M. C. 2019, *A&A*, 629, A124. doi:10.1051/0004-6361/201834818
- Martinez, L., Bersten, M. C., Anderson, J. P., et al. 2020, *A&A*, 642, A143. doi:10.1051/0004-6361/202038393
- Martinez, L., Bersten, M. C., Anderson, J. P., et al. 2022, *A&A*, 660, A40. doi:10.1051/0004-6361/202142075
- Martinez, L., Bersten, M. C., Anderson, J. P., et al. 2022, *A&A*, 660, A41. doi:10.1051/0004-6361/202142076
- Martinez, L., Anderson, J. P., Bersten, M. C., et al. 2022, *A&A*, 660, A42. doi:10.1051/0004-6361/202142555
- Matsuoka, T. & Sawada, R. 2023, arXiv:2307.00727. doi:10.48550/arXiv.2307.00727
- Maund, J. R. & Smartt, S. J. 2005, *MNRAS*, 360, 288. doi:10.1111/j.1365-2966.2005.09034.x
- Maund, J. R., Smartt, S. J., & Danziger, I. J. 2005, *MNRAS*, 364, L33. doi:10.1111/j.1745-3933.2005.00100.x
- Maund, J. R. & Smartt, S. J. 2009, *Science*, 324, 486. doi:10.1126/science.1170198
- Maund, J. R., Fraser, M., Smartt, S. J., et al. 2013, *MNRAS*, 431, L102. doi:10.1093/mnrasl/slt017
- Maund, J. R., Reilly, E., & Mattila, S. 2014, *MNRAS*, 438, 938. doi:10.1093/mnras/stt2131
- Maund, J. R., Mattila, S., Ramirez-Ruiz, E., et al. 2014, *MNRAS*, 438, 1577. doi:10.1093/mnras/stt2296
- Meynet, G., Chomienne, V., Ekström, S., et al. 2015, *A&A*, 575, A60. doi:10.1051/0004-6361/201424671
- Modjaz, M., Gutiérrez, C. P., & Arcavi, I. 2019, *Nature Astronomy*, 3, 717. doi:10.1038/s41550-019-0856-2
- Moriya, T. J., Pruzhinskaya, M. V., Ergon, M., et al. 2016, *MNRAS*, 455, 423. doi:10.1093/mnras/stv2336
- Moriya, T. J., Subrayan, B. M., Milisavljevic, D., et al. 2023, arXiv:2303.01532. doi:10.48550/arXiv.2303.01532
- Morozova, V., Piro, A. L., Renzo, M., et al. 2015, *ApJ*, 814, 63. doi:10.1088/0004-637X/814/1/63
- Morozova, V., Piro, A. L., Renzo, M., et al. 2016, *ApJ*, 829, 109. doi:10.3847/0004-637X/829/2/109
- Morozova, V., Piro, A. L., & Valenti, S. 2017, *ApJ*, 838, 28. doi:10.3847/1538-4357/aa6251
- Morozova, V., Piro, A. L., & Valenti, S. 2018, *ApJ*, 858, 15. doi:10.3847/1538-4357/aab9a6
- Murai, Y., Tanaka, M., Kawabata, M., et al. 2024, *MNRAS*, 528, 4209. doi:10.1093/mnras/stae170
- Nagao, T., Cikota, A., Patat, F., et al. 2019, *MNRAS*, 489, L69. doi:10.1093/mnrasl/slz119
- Nagao, T., Patat, F., Taubenberger, S., et al. 2021, *MNRAS*, 505, 3664. doi:10.1093/mnras/stab1582
- Nieuwenhuijzen, H. & de Jager, C. 1990, *A&A*, 231, 134
- Nugis, T. & Lamers, H. J. G. L. M. 2000, *A&A*, 360, 227
- Nugis, T. & Lamers, H. J. G. L. M. 2002, *A&A*, 389, 162. doi:10.1051/0004-6361:20020557
- Olivares E., F., Hamuy, M., Pignata, G., et al. 2010, *ApJ*, 715, 833. doi:10.1088/0004-637X/715/2/833
- O'Neill, D., Kotak, R., Fraser, M., et al. 2019, *A&A*, 622, L1. doi:10.1051/0004-6361/201834566
- Ouchi, R. & Maeda, K. 2017, *ApJ*, 840, 90. doi:10.3847/1538-4357/aa6ea9
- Pastorello, A., Valenti, S., Zampieri, L., et al. 2009, *MNRAS*, 394, 2266. doi:10.1111/j.1365-2966.2009.14505.x

- Poznanski, D., Butler, N., Filippenko, A. V., et al. 2009, *ApJ*, 694, 1067. doi:10.1088/0004-637X/694/2/1067
- Paxton, B., Bildsten, L., Dotter, A., et al. 2011, *ApJS*, 192, 3. doi:10.1088/0067-0049/192/1/3
- Paxton, B., Cantiello, M., Arras, P., et al. 2013, *ApJS*, 208, 4. doi:10.1088/0067-0049/208/1/4
- Paxton, B., Marchant, P., Schwab, J., et al. 2015, *ApJS*, 220, 15. doi:10.1088/0067-0049/220/1/15
- Paxton, B., Schwab, J., Bauer, E. B., et al. 2018, *ApJS*, 234, 34. doi:10.3847/1538-4365/aaa5a8
- Paxton, B., Smolec, R., Schwab, J., et al. 2019, *ApJS*, 243, 10. doi:10.3847/1538-4365/ab2241
- Prentice, S. J., Ashall, C., James, P. A., et al. 2019, *MNRAS*, 485, 1559. doi:10.1093/mnras/sty3399
- Reguitti, A., Pumo, M. L., Mazzali, P. A., et al. 2021, *MNRAS*, 501, 1059. doi:10.1093/mnras/staa3730
- Pignata, G. 2013, *Massive Stars: From alpha to Omega*, 176
- Popov, D. V. 1993, *ApJ*, 414, 712. doi:10.1086/173117
- Reimers, D. 1975, *Memoires of the Societe Royale des Sciences de Liege*, 8, 369
- Rodríguez, Ó., Meza, N., Pineda-García, J., et al. 2021, *MNRAS*, 505, 1742. doi:10.1093/mnras/stab1335
- Roy, R., Kumar, B., Benetti, S., et al. 2011, *ApJ*, 736, 76. doi:10.1088/0004-637X/736/2/76
- Rui, L., Wang, X., Mo, J., et al. 2019, *MNRAS*, 485, 1990. doi:10.1093/mnras/stz503
- Salpeter, E. E. 1955, *ApJ*, 121, 161. doi:10.1086/145971
- Sana, H., de Mink, S. E., de Koter, A., et al. 2012, *Science*, 337, 444. doi:10.1126/science.1223344
- Schröder, K.-P. & Cuntz, M. 2005, *ApJL*, 630, L73. doi:10.1086/491579
- Singh, A., Kumar, B., Moriya, T. J., et al. 2019, *ApJ*, 882, 68. doi:10.3847/1538-4357/ab3050
- Smartt, S. J., Maund, J. R., Hendry, M. A., et al. 2004, *Science*, 303, 499. doi:10.1126/science.1092967
- Smartt, S. J. 2009, *ARA&A*, 47, 63. doi:10.1146/annurev-astro-082708-101737
- Smartt, S. J. 2015, *PASA*, 32, e016. doi:10.1017/pasa.2015.17
- Smith, N., Li, W., Filippenko, A. V., et al. 2011, *MNRAS*, 412, 1522. doi:10.1111/j.1365-2966.2011.17229.x
- Smith, N. 2014, *ARA&A*, 52, 487. doi:10.1146/annurev-astro-081913-040025
- Sollerman, J., Yang, S., Schulze, S., et al. 2021, *A&A*, 655, A105. doi:10.1051/0004-6361/202141374
- Spiro, S., Pastorello, A., Pumo, M. L., et al. 2014, *MNRAS*, 439, 2873. doi:10.1093/mnras/stu156
- Strotjohann, N. L., Ofek, E. O., & Gal-Yam, A. 2023, *arXiv:2311.00744*. doi:10.48550/arXiv.2311.00744
- Subrayan, B. M., Milisavljevic, D., Moriya, T. J., et al. 2023, *ApJ*, 945, 46. doi:10.3847/1538-4357/aca80a
- Sukhbold, T., Ertl, T., Woosley, S. E., et al. 2016, *ApJ*, 821, 38. doi:10.3847/0004-637X/821/1/38
- Sun, N.-C., Maund, J. R., & Crowther, P. A. 2023, *MNRAS*. doi:10.1093/mnras/stad690
- Szalai, T., Vinkó, J., Könyves-Tóth, R., et al. 2019, *ApJ*, 876, 19. doi:10.3847/1538-4357/ab12d0
- Takahashi, K., Takiwaki, T., & Yoshida, T. 2023, *ApJ*, 945, 19. doi:10.3847/1538-4357/acb8b3
- Takáts, K. & Vinkó, J. 2006, *MNRAS*, 372, 1735. doi:10.1111/j.1365-2966.2006.10974.x
- Takáts, K., Pumo, M. L., Elias-Rosa, N., et al. 2014, *MNRAS*, 438, 368. doi:10.1093/mnras/stt2203
- Takáts, K., Pignata, G., Pumo, M. L., et al. 2015, *MNRAS*, 450, 3137. doi:10.1093/mnras/stv857
- Tartaglia, L., Sand, D. J., Groh, J. H., et al. 2021, *ApJ*, 907, 52. doi:10.3847/1538-4357/abca8a
- Teja, R. S., Singh, A., Sahu, D. K., et al. 2022, *ApJ*, 930, 34. doi:10.3847/1538-4357/ac610b
- Teja, R. S., Singh, A., Sahu, D. K., et al. 2023, *arXiv:2306.10136*. doi:10.48550/arXiv.2306.10136
- Temaj, D., Schneider, F. R. N., Laplace, E., et al. 2023, *arXiv:2311.05701*. doi:10.48550/arXiv.2311.05701
- Terreran, G., Jerkstrand, A., Benetti, S., et al. 2016, *MNRAS*, 462, 137. doi:10.1093/mnras/stw1591
- Terreran, G., Margutti, R., Bersier, D., et al. 2019, *ApJ*, 883, 147. doi:10.3847/1538-4357/ab3e37
- Tomasella, L., Cappellaro, E., Fraser, M., et al. 2013, *MNRAS*, 434, 1636. doi:10.1093/mnras/stt1130
- Tomasella, L., Cappellaro, E., Pumo, M. L., et al. 2018, *MNRAS*, 475, 1937. doi:10.1093/mnras/stx3220
- Tsvetkov, D. Y., Volnova, A. A., Shulga, A. P., et al. 2006, *A&A*, 460, 769. doi:10.1051/0004-6361:20065704
- Tsvetkov, D. Y., Goranskij, V., & Pavlyuk, N. 2008, *Peremennye Zvezdy*, 28, 8. doi:10.48550/arXiv.0810.3988
- Tsvetkov, D. Y., Shugarov, S. Y., Volkov, I. M., et al. 2018, *Astronomy Letters*, 44, 315. doi:10.1134/S1063773718050043
- Tsvetkov, D. Y., Goranskij, V. P., Barsukova, E. A., et al. 2022, *Astrophysical Bulletin*, 77, 407. doi:10.1134/S1990341322040162
- Utrobin, V. P. & Chugai, N. N. 2009, *A&A*, 506, 829. doi:10.1051/0004-6361/200912273
- Utrobin, V. P., Chugai, N. N., Andrews, J. E., et al. 2021, *MNRAS*, 505, 116. doi:10.1093/mnras/stab1369
- Van Dyk, S. D., Li, W., & Filippenko, A. V. 2003, *PASP*, 115, 1289. doi:10.1086/378308
- Van Dyk, S. D., Davidge, T. J., Elias-Rosa, N., et al. 2012, *AJ*, 143, 19. doi:10.1088/0004-6256/143/1/19

- Van Dyk, S. D., Cenko, S. B., Poznanski, D., et al. 2012, *ApJ*, 756, 131. doi:10.1088/0004-637X/756/2/131
- Van Dyk, S. D., Zheng, W., Maund, J. R., et al. 2019, *ApJ*, 875, 136. doi:10.3847/1538-4357/ab1136
- Van Dyk, S. D., de Graw, A., Baer-Way, R., et al. 2023, *MNRAS*, 519, 471. doi:10.1093/mnras/stac3549
- Van Dyk, S. D., Bostroem, K. A., Andrews, J. E., et al. 2023, arXiv:2302.00274. doi:10.48550/arXiv.2302.00274
- van Loon, J. T., Cioni, M.-R. L., Zijlstra, A. A., et al. 2005, *A&A*, 438, 273. doi:10.1051/0004-6361:20042555
- Valenti, S., Sand, D., Pastorello, A., et al. 2014, *MNRAS*, 438, L101. doi:10.1093/mnrasl/slt171
- Valenti, S., Sand, D., Stritzinger, M., et al. 2015, *MNRAS*, 448, 2608. doi:10.1093/mnras/stv208
- Valenti, S., Howell, D. A., Stritzinger, M. D., et al. 2016, *MNRAS*, 459, 3939. doi:10.1093/mnras/stw870
- Vasylyev, S. S., Filippenko, A. V., Vogl, C., et al. 2022, *ApJ*, 934, 134. doi:10.3847/1538-4357/ac7220
- Villar, V. A., Berger, E., Metzger, B. D., et al. 2017, *ApJ*, 849, 70. doi:10.3847/1538-4357/aa8fcb
- Vink, J. S., de Koter, A., & Lamers, H. J. G. L. M. 2001, *A&A*, 369, 574. doi:10.1051/0004-6361:20010127
- Vinkó, J., Takáts, K., Sárneczky, K., et al. 2006, *MNRAS*, 369, 1780. doi:10.1111/j.1365-2966.2006.10416.x
- Vinkó, J., Sárneczky, K., Balog, Z., et al. 2009, *ApJ*, 695, 619. doi:10.1088/0004-637X/695/1/619
- Vink, J. S. & Sabhahit, G. N. 2023, *A&A*, 678, L3. doi:10.1051/0004-6361/202347801
- Virtanen, P., Gommers, R., Oliphant, T. E., et al. 2020, *Nature Methods*, 17, 261. doi:10.1038/s41592-019-0686-2
- Walmswell, J. J. & Eldridge, J. J. 2012, *MNRAS*, 419, 2054. doi:10.1111/j.1365-2966.2011.19860.x
- Wheeler, J. C., Johnson, V., & Clocchiatti, A. 2015, *MNRAS*, 450, 1295. doi:10.1093/mnras/stv650
- Willson, L. A. 2000, *ARA&A*, 38, 573. doi:10.1146/annurev.astro.38.1.573
- Woosley, S. E. 1988, *ApJ*, 330, 218. doi:10.1086/166468
- Yaron, O., Perley, D. A., Gal-Yam, A., et al. 2017, *Nature Physics*, 13, 510. doi:10.1038/nphys4025
- Yoon, S.-C., Woosley, S. E., & Langer, N. 2010, *ApJ*, 725, 940. doi:10.1088/0004-637X/725/1/940
- Yoon, S.-C. 2015, *PASA*, 32, e015. doi:10.1017/pasa.2015.16
- Yoon, S.-C., Dessart, L., & Clocchiatti, A. 2017, *ApJ*, 840, 10. doi:10.3847/1538-4357/aa6afe
- Zha, S., Müller, B., Weir, A., et al. 2023, *ApJ*, 952, 155. doi:10.3847/1538-4357/acd845
- Zhang, T., Wang, X., Li, W., et al. 2006, *AJ*, 131, 2245. doi:10.1086/500972
- Zhang, J., Wang, X., József, V., et al. 2020, *MNRAS*, 498, 84. doi:10.1093/mnras/staa2273
- Zhang, X., Wang, X., Sai, H., et al. 2022, *MNRAS*, 509, 2013. doi:10.1093/mnras/stab3007